Inorg. Chem. **2006**, *45*, 529–546

Fast Magnetization Tunneling in Tetranickel(II) Single-Molecule Magnets

En-Che Yang,[†] Wolfgang Wernsdorfer,[‡] Lev N. Zakharov,[†] Yoshitomo Karaki,[§] Akira Yamaguchi,[§] Rose M. Isidro,[†] Guo-Di Lu,[†] Samuel A. Wilson,[†] Arnold L. Rheingold,[†] Hidehiko Ishimoto,[§] and David N. Hendrickson*,[†]

Department of Chemistry and Biochemistry, University of California at San Diego, La Jolla, California 92093-0358, Laboratoire Louis Néel-CNRS, 25 Avenue des Martyrs, 38042 Grenoble Cedex 9, France, and Institute of Solid State Physics, The University of Tokyo, Kashiwanoha 5-1-5, Kashiwa, Chiba 277-8581, Japan

Received January 20, 2005

A series of Ni_4 cubane complexes with the composition $[Ni(hmp)(ROH)Cl]_4$ complexes **1**–**4** where R= $-CH_3$ (complex **1**), $-CH_2CH_3$ (complex **2**), $-CH_2CH_2(C_4H_9)$ (complex **3**), $-CH_2CH_2CH_2(C_6H_{11})$ (complex **4**), hmp^- is the anion of 2-hydroxymethylpyridine, *t*-$Buhmp^-$ is the anion of 4-*tert*-butyl-2-hydroxymethylpyridine, and dmb is 3,3-dimethyl-1-butanol] and $[Ni(hmp)(dmb)Br]_4$ (complex **5**) and $[Ni(t\text{-}Buhmp)(dmb)Cl]_4$ (complex **6**) were prepared. All six complexes were characterized by dc magnetic susceptibility data to be ferromagnetically coupled to give an $S = 4$ ground state with significant magnetoanisotropy ($D \approx -0.6$ cm^{-1}). Magnetization hysteresis measurements carried out on single crystals of complexes **1**–**6** establish the single-molecule magnet (SMM) behavior of these complexes. The exchange bias observed in the magnetization hysteresis loops of complexes **1** and **2** is dramatically decreased to zero in complex **3**, where the bulky dmb ligand is employed. Fast tunneling of magnetization is observed for the high-symmetry (S_4 site symmetry) Ni_4 complexes in the crystal of complex **3**, and the tunneling rate can even be enhanced by destroying the S_4 site symmetry, as is the case for complex **4**, where there are two crystallographically different Ni_4 molecules, one with C_2 and the other with C_1 site symmetry. Magnetic ordering temperatures due to intermolecular dipolar and magnetic exchange interactions were determined by means of very low-temperature ac susceptibility measurements; complex **1** orders at 1100 mK, complex **3** at 290 mK, complex **4** at ∼80 mK, and complex **6** at <50 mK. This confirms that bulkier ligands correspond to more isolated molecules, and therefore, magnetic ordering occurs at lower temperatures for those complexes with the bulkiest ligands.

Introduction

There is a growing interest in single-molecule magnets (SMMs), molecules that function as nanomagnets.[1−4] The three requirements for a molecule to be an SMM are (1) a high-spin *S* ground state, (2) appreciable negative magnetoanisotropy, and (3) a weak tunnel splitting that leads to quantum tunneling of the direction of magnetization. Because all of the molecules in a crystal of an SMM have the same size, spin, shape, and magnetoanisotropy, it has been possible for the first time to characterize the quantum effects associated with the magnetization dynamics of nanomagnets. The quantum effects that have been studied for SMMs include tunneling of the direction of magnetization,[5,6] quantum phase interference,[7,8] and spin parity effects.[9−11]

* To whom correspondence should be addressed. Fax: 1-858-534-5383. E-mail: dhendrickson@ucsd.edu.
[†] University of California at San Diego.
[‡] Laboratoire Louis Néel-CNRS.
[§] The University of Tokyo.

(1) Gatteschi, D.; Sessoli, R. *Angew. Chem., Int. Ed.* **2003**, *42* (3), 268−297.
(2) Sessoli, R.; Tsai, H. L.; Schake, A. R.; Wang, S. Y.; Vincent, J. B.; Folting, K.; Gatteschi, D.; Christou, G.; Hendrickson, D. N. *J. Am. Chem. Soc.* **1993**, *115* (5), 1804−1816.
(3) Christou, G.; Gatteschi, D.; Hendrickson, D. N.; Sessoli, R. *MRS Bull.* **2000**, *25* (11), 66−71.
(4) Sessoli, R.; Gatteschi, D.; Caneschi, A.; Novak, M. A. *Nature* **1993**, *365* (6442), 141−143.
(5) Friedman, J. R.; Sarachik, M. P.; Tejada, J.; Ziolo, R. *Phys. Rev. Lett.* **1996**, *76* (20), 3830−3833.
(6) Thomas, L.; Lionti, F.; Ballou, R.; Gatteschi, D.; Sessoli, R.; Barbara, B. *Nature* **1996**, *383* (6596), 145−147.
(7) Wernsdorfer, W.; Chiorescu, I.; Sessoli, R.; Gatteschi, D.; Mailly, D. *Physica B* **2000**, *284*, 1231−1232.
(8) Wernsdorfer, W.; Sessoli, R.; Caneschi, A.; Gatteschi, D.; Cornia, A.; Mailly, D. *J. Appl. Phys.* **2000**, *87* (9), 5481−5486.
(9) Wernsdorfer, W.; Bhaduri, S.; Boskovic, C.; Christou, G.; Hendrickson, D. N. *Phys. Rev. B* **2002**, *65* (18), 180403.

10.1021/ic050093r CCC: $33.50 © 2006 American Chemical Society
Published on Web 12/16/2005

Many different directions are being pursued in the study of SMMs, including attaching SMMs to surfaces.[12−14] SMMs that have the largest spin ground state are one focus. In 2000, Goodwin et al.[15,16] reported an Fe_{19} SMM with $S = 33/2$ and axial zero-field splitting of $D = -0.56$ K that exhibits magnetization hysteresis at temperatures below 1 K. Two years later, Andres et al.[17] reported a Ni_{12} complex that is an SMM with $S = 12$ and $D = -0.067$ K that shows magnetization hysteresis below 0.40 K. A $[Mn_{18}]^{2+}$ SMM with $S = 13$ and $D = -0.13$ cm^{-1} was also reported in 2002 by Brechin et al.[18] Finally, in 2004, Murugesu et al.[19] reported an SMM with the highest spin of $S = 51/2$. This $S = 51/2$ complex has a Mn_{25} composition with $D = -0.032$ K, which gives an upper limit to the magnetization relaxation barrier of $(S^2 - {}^1/_4)|D| = 21$ K. Magnetization hysteresis was observed for a single crystal below ~0.6 K. Increasing the molecular size is another goal in the research on SMMs. However, it has been found that simply increasing the number of metal ions in a given molecule does not lead to an increase in S. For example, a Mn_{30} SMM has been reported to have only $S = 5$ in the ground state ($D = -0.73$ K) with a blocking temperature of ~1.4 K.[20] The largest SMM was recently reported as a 4-nm-diameter torus-shaped Mn_{84} SMM.[21] Magnetic susceptibility studies down to 0.04 K indicate that the ground state has $S = 6$, and magnetization hysteresis was observed below 1.5 K. Below 0.2 K, the rate of magnetization relaxation is temperature-independent for this Mn_{84} SMM, which clearly establishes the presence of quantum tunneling of magnetization (QTM) in this large SMM.

Another direction in SMM research involves detailed studies of the mechanism of magnetization tunneling. It has been found that Kramers degeneracy affects the tunnel splitting in half-integer-spin SMMs such as the $S = {}^9/_2$ Mn_4 cubane complexes.[10] The small internal magnetic field associated with nuclear spins was also found to have an appreciable effect.[10,22,23] Very recently, the nature of the transverse interactions responsible for QTM in the first SMM, $[Mn_{12}O_{12}(O_2CCH_3)_{16}(H_2O)_4]\cdot 2(CH_3CO_2H)\cdot 4(H_2O)$, called Mn_{12}−Ac, has been established.[24−26] The site symmetry for the Mn_{12} SMM in a crystal of Mn_{12}−Ac is S_4, and for 10 years, the origin of QTM in this complex was an open question. Although Mn_{12}−Ac has an apparent high symmetry, QTM does not reflect this symmetry, which leads to selection rules in QTM that are not observed. QTM was established by detailed high-field electron paramagnetic resonance (HFEPR) spectroscopy and micro-Hall magnetometry to be due to discrete solvate molecule disorder in the crystal. The water and acetic acid solvate molecules are disordered and provide for Mn_{12} molecules with different environments, so-called microenvironments.

In other studies of the mechanism of QTM in SMMs, it has been found that intermolecular magnetic exchange interactions are important.[27−29] Detailed magnetization data were presented for $[Mn_4O_3Cl_4(O_2CEt)_3(py)_3]_2$ (py is pyridine), a supramolecular dimer of two $S = {}^9/_2$ Mn_4 SMMs held together in a head-to-head fashion by a Cl···Cl contact and six weak C−H···Cl hydrogen bonds. These intermolecular contacts result in an antiferromagnetic exchange interaction ($J = -0.05$ K) between the two $S = {}^9/_2$ Mn_4 molecules. This interaction leads to an "exchange bias" in the magnetic field at which QTM occurs. When one $S = {}^9/_2$ complex is undergoing a QTM event, flipping its magnetization vector from "spin up" to "spin down", it does so under the influence of the weak antiferromagnetic interaction with its neighboring molecule.

The above observations about the effects of intermolecular magnetic exchange interactions upon QTM led us to prepare a series of SMMs where we could use chemistry to modify the intermolecular interactions. A series of SMMs was sought where the ground-state spin S was not too large and would facilitate the application of HFEPR to determine the spin Hamiltonian parameters characterizing SMMs. Preliminary data have been reported[30] for a few complexes of the composition $[Ni(hmp)(ROH)X]_4$, where hmp^- is the anion

(10) Aubin, S. M. J.; Dilley, N. R.; Pardi, L.; Krzystek, J.; Wemple, M. W.; Brunel, L. C.; Maple, M. B.; Christou, G.; Hendrickson, D. N. *J. Am. Chem. Soc.* **1998**, *120* (20), 4991−5004.

(11) Wernsdorfer, W.; Sessoli, R. *Science* **1999**, *284* (5411), 133−135.

(12) Ruiz-Molina, D.; Mas-Torrent, M.; Gomez, J.; Balana, A. I.; Domingo, N.; Tejada, J.; Martinez, M. T.; Rovira, C.; Veciana, J. *Adv. Mater.* **2003**, *15* (1), 42.

(13) Cornia, A.; Fabretti, A. C.; Pacchioni, M.; Zobbi, L.; Bonacchi, D.; Caneschi, A.; Gatteschi, D.; Biagi, R.; Del Pennino, U.; De Renzi, V.; Gurevich, L.; Van der Zant, H. S. J. *Angew. Chem., Int. Ed.* **2003**, *42* (14), 1645−1648.

(14) Clemente-Leon, M.; Soyer, H.; Coronado, E.; Mingotaud, C.; Gomez-Garcia, C. J.; Delhaes, P. *Angew. Chem., Int. Ed.* **1998**, *37* (20), 2842−2845.

(15) Goodwin, J. C.; Sessoli, R.; Gatteschi, D.; Wernsdorfer, W.; Powell, A. K.; Heath, S. L. *J. Chem. Soc., Dalton Trans.* **2000**, (12), 1835−1840.

(16) Goodwin, J. C.; Sessoli, R.; Gatteschi, D.; Wernsdorfer, W.; Powell, A. K.; Heath, S. L.; Barra, A. L. *J. Chem. Soc., Dalton Trans.* **2000**, (24), 4702−4702.

(17) Andres, H.; Basler, R.; Blake, A. J.; Cadiou, C.; Chaboussant, G.; Grant, C. M.; Gudel, H. U.; Murrie, M.; Parsons, S.; Paulsen, C.; Semadini, F.; Villar, V.; Wernsdorfer, W.; Winpenny, R. E. P. *Chem.−Eur. J.* **2002**, *8* (21), 4867−4876.

(18) Brechin, E. K.; Boskovic, C.; Wernsdorfer, W.; Yoo, J.; Yamaguchi, A.; Sanudo, E. C.; Concolino, T. R.; Rheingold, A. L.; Ishimoto, H.; Hendrickson, D. N.; Christou, G. *J. Am. Chem. Soc.* **2002**, *124* (33), 9710−9711.

(19) Murugesu, M.; Habrych, M.; Wernsdorfer, W.; Abboud, K. A.; Christou, G. *J. Am. Chem. Soc.* **2004**, *126* (15), 4766−4767.

(20) Soler, M.; Wernsdorfer, W.; Folting, K.; Pink, M.; Christou, G. *J. Am. Chem. Soc.* **2004**, *126* (7), 2156−2165.

(21) Tasiopoulos, A. J.; Vinslava, A.; Wernsdorfer, W.; Abboud, K. A.; Christou, G. *Angew. Chem., Int. Ed.* **2004**, *43* (16), 2117−2121.

(22) Wernsdorfer, W.; Sessoli, R.; Gatteschi, D. *Europhys. Lett.* **1999**, *47* (2), 254−259.

(23) Wernsdorfer, W.; Caneschi, A.; Sessoli, R.; Gatteschi, D.; Cornia, A.; Villar, V.; Paulsen, C. *Phys. Rev. Lett.* **2000**, *84* (13), 2965−2968.

(24) (a) del Barco, E.; Kent, A. D.; Chakov, N. E.; Zakharov, L. N.; Rheingold, A. L.; Hendrickson, D. N.; Christou, G. *Phys. Rev. B* **2004**, *69* (2), 020411(R). (b) Hill, S.; Macagnano, S.; Park, K.; Achey, R. M.; North, J. M.; Dalal, N. S. *Phys. Rev. B* **2002**, *65*, 224410. (c) Park, K.; Novotny, M. A.; Dalal, N. S.; Hill, S.; Rikvold, P. A. *Phys. Rev. B* **2001**, *65*, 014426.

(25) Amigo, R.; del Barco, E.; Casas, L.; Molins, E.; Tejada, J.; Rutel, I. B.; Mommouton, B.; Dalal, N.; Brooks, J. *Phys. Rev. B* **2002**, *65* (17), 172403.

(26) Hill, S.; Edwards, R. S.; Jones, S. I.; Dalal, N. S.; North, J. M. *Phys. Rev. Lett.* **2003**, *90* (21), 217204.

(27) Wernsdorfer, W.; Ohm, T.; Sangregorio, C.; Sessoli, R.; Gatteschi, D.; Paulsen, C. *Physica B* **2000**, *284*, 1229−1230.

(28) Wernsdorfer, W.; Bhaduri, S.; Tiron, R.; Hendrickson, D. N.; Christou, G. *Phys. Rev. Lett.* **2002**, *89* (19), 197201.

(29) Wernsdorfer, W.; Allaga-Alcalde, N.; Hendrickson, D. N.; Christou, G. *Nature* **2002**, *416* (6879), 406−409.

of 2-hydroxymethylpyridine, R is some alkyl substituent, and X^- is either Cl^- or Br^-. In this article, we report on an extensive series of these Ni_4 SMMs, where the R substituent and halide ligand are varied to modulate weak intermolecular magnetic exchange interactions. Within each Ni^{II}_4 molecule, there are relatively strong ferromagnetic interactions between neighboring Ni^{II} ions, giving an $S = 4$ ground state. Several goals have been set in our studies of these $S = 4$ tetranickel SMMs. First, it is interesting to see how changes in the R substituent or a *tert*-butyl group added to the hmp^- ligand modulate intermolecular magnetic exchange interactions and how this is manifested in the magnetization vs magnetic field hysteresis loops for these SMMs. Second, the rate of ground-state QTM is relatively high in these Ni_4 SMMs, and it is important to understand the origin of the fast QTM. A longer-range goal is to study the decoherence rate of QTM in these Ni_4 SMMs.[31] The preparation, X-ray structures, magnetization hysteresis, and dc and ac magnetization data are reported in this paper for six Ni_4 SMMs. Very low-temperature (from ~50 mK to ~1.5 K) ac/dc magnetization data were obtained to characterize the magnetic ordering in these Ni_4 SMMs. In later articles, HFEPR data will be analyzed to characterize magnetization reversal in individual molecules and spin Hamiltonian parameters for an analogous Zn_3Ni complex crystal and for the crystals of nondoped Ni_4 SMMs.

Experimental Section

Synthesis. All manipulations were performed under aerobic conditions. The ligand 4-*tert*-butyl-2-hydroxymethylpyridine (*t*-BuhmpH) was synthesized as reported in the literature.[32]

$[Ni(hmp)(MeOH)Cl]_4$ (1). A mixture of $NiCl_2 \cdot 4H_2O$ (4.75 g, 20 mmol), 2-hydroxymethylpyridine (hmpH) (2.18 g, 20 mmol), and NaOMe (1.08 g, 20 mmol) in 100 mL of MeOH was refluxed for 30 min. The resulting solution was filtered when it was still hot. Green crystals suitable for X-ray analysis were then collected after the solution cooled; the yield was 20%. Anal. Calcd (found) for $Ni_4C_{28}N_4H_{42}O_9Cl_4$: C, 35.4 (35.4); H, 4.46 (4.37); N, 5.90 (5.80). Selected IR data (KBr, cm^{-1}): 3340 (br, s), 2906 (w), 2841 (m), 1605 (s), 1480 (s), 1442 (s), 1360 (m), 1284 (s), 1219 (w), 1153 (m), 1071 (s), 821 (w), 761 (m), 722 (m), 646 (m).

$[Ni(hmp)(EtOH)Cl]_4$ (2). A mixture of $NiCl_2 \cdot 4H_2O$ (4.75 g, 20 mmol), 2-hydroxymethylpyridine (hmpH) (2.18 g, 20 mmol), and NaOEt (1.36 g, 20 mmol) in 100 mL of EtOH was refluxed for 30 min. The resulting solution was filtered when it is still hot. Green crystals suitable for X-ray analysis were then obtained after the solution cooled; the yield was 30%. Anal. Calcd (found) for $Ni_4C_{32}N_4H_{50}O_9Cl_4$: C, 38.2 (38.3); H, 5.01 (4.71); N, 5.57 (5.56). Selected IR data (KBr, cm^{-1}): 3337 (br, s), 2907 (w), 2842 (m), 1605 (s), 1480 (s), 1442 (s), 1366 (m), 1284 (s), 1219 (w), 1153 (m), 1071 (s), 815 (w), 761 (m), 727 (m), 646 (m).

$[Ni(hmp)(dmb)Cl]_4$ (3). Complex **1** (3.9 g) was dissolved in a solution of 50 g of 3,3-dimethyl-1-butanol (dmb) and 60 mL of methylenechloride. After filtration, the solution was allowed to evaporate slowly. Green-colored crystals suitable for X-ray structure analysis were obtained; the yield was 80%. Anal. Calcd (found) for $Ni_4C_{48}N_4H_{80}O_8Cl_4$: C, 47.5 (47.1); H, 6.65 (6.10); N, 4.62 (4.59). Selected IR data (KBr, cm^{-1}): 3212 (s), 2956 (s), 2902 (s), 1606 (s), 1567 (s), 1480 (s), 1442 (s), 1398 (m), 1366 (s), 1284 (s), 1246 (m), 1153 (s), 1077 (s), 1044 (s), 995 (m), 968 (w), 815 (w), 750 (s), 729 (s), 646 (s).

$[Ni(hmp)(chp)Cl]_4$ (4). Complex **1** (2.5 g) was dissolved in a solution of 50 g of 3-cyclohexyl-1-propanol (chp) and 40 mL of methylenechloride. After filtration, the solution was allowed to evaporate slowly. Green-colored crystals suitable for X-ray structural analysis were obtained; the yield was 50%. Anal. Calcd (found) for $Ni_4C_{60}N_4H_{96}O_8Cl_4$: C, 52.5 (52.65); H, 7.05 (6.64); N, 4.08 (3.89). Selected IR data (KBr, cm^{-1}): 3218 (s), 2918 (s), 2842 (s), 1605 (s), 1570 (s), 1481 (s), 1443 (s), 1399 (s), 1360 (m), 1287 (s), 1233 (w), 1151 (s), 1071 (s), 1020 (s), 957 (m), 890 (m), 820 (m), 760 (s), 725 (s), 649 (s), 502 (s).

$[Ni(hmp)(dmb)Br]_4$ (5). Complex **5** was prepared by a procedure similar to that employed for complex **3**, except that the metal salt $NiCl_2 \cdot 4H_2O$ was replaced with $NiBr_2 \cdot 4H_2O$. The yield was 20%. Anal. Calcd (found) for $Ni_4C_{48}N_4H_{80}O_8Br_4$: C, 41.5 (41.22); H, 5.81 (5.79); N, 4.04 (3.97). Selected IR data (KBr, cm^{-1}): 3245 (s), 2951 (s), 2895 (s), 1605 (s), 1570 (s), 1478 (s), 1443 (s), 1395 (s), 1364 (s), 1284 (s), 1243 (m), 1154 (s), 1075 (s), 1046 (s), 998 (s), 966 (m), 919 (w), 887 (w), 820 (m), 754 (s), 731 (s), 649 (s), 502 (s), 464 (s).

$[Ni(t\text{-}Buhmp)(dmb)Cl]_4$ (6). Complex **6** was prepared by a procedure similar to that employed for complex **3**, except that the ligand hmpH was replaced by *t*-BuhmpH. The yield was 25%. Anal. Calcd (found) for $Ni_4C_{48}N_4H_{80}O_8Br_4$: C, 53.5 (53.5); H, 7.86 (8.16); N, 3.90 (3.86). Selected IR data (KBr, cm^{-1}): 3223 (s), 2962 (s), 1615 (s), 1551 (m), 1475 (s), 1405 (s), 1364 (s), 1344 (m), 1294 (m), 1249 (m), 1202 (m), 1170 (w), 1084 (s), 1043 (s), 992 (m), 894 (m), 836 (m), 728 (m), 677 (m), 604 (m), 544 (w), 518 (m).

X-ray Crystallography. Diffraction data were collected at low temperatures with Bruker Smart Apex CCD (**1**−**4**) and Bruker P4/CCC (**5**,**6**) diffractometers equipped with Mo Kα radiation (λ = 0.71073 Å). Absorption corrections were applied by SADABS for all data. The structures were solved by direct methods and refined on F^2 (SHELXTL, version 6.10, Bruker AXS, Inc., Madison, WI, 2000) by a full-matrix least-squares procedure. All non-hydrogen atoms were refined anisotropically, except for the C atoms of disordered CH_2 groups in ROH ligands (**4**), which were refined isotropically. All H atoms in **3** and **5** and H atoms at O atoms in the ROH groups in **1** and **6** involved in the hydrogen bonds were found on the residual density and refined with isotropic thermal parameters. Other H atoms in **1** and **6** and all H atoms in **2** and **4** were treated in calculated idealized positions. The H atoms of disordered CH_2 groups in **4** were not taken into consideration. The CH_2 groups in **4** and some methyl groups in **6** are disordered over two positions. In addition to the Ni_4 molecules, solvent water molecules were found in crystal structures of **1** (disordered over two positions around a center of symmetry) and **2** (on a 2-fold axis). Peaks on the *F* maps corresponding to these water molecules in **1** and **2** are not strong and indicate that these water positions in the crystal structures are not fully occupied. The Flack parameters for noncentrosymmetric structures are 0.08(3) (**1**), 0.00(2) (**2**), and 0.06(2) (**6**). Crystallographic data and details of the X-ray study are reported in Tables 1−3. All software and sources of scattering factors are contained in the SHELXTL (6.10) program package (G. Sheldrick, Bruker XRD, Madison, WI).

Other Physical Property Measurements. Orientated single-crystal magnetization hysteresis loops were measured by employing a micro-SQUID array that has been described elsewhere.[33] A single

(30) Yang, E. C.; Wernsdorfer, W.; Hill, S.; Edwards, R. S.; Nakano, M.; Maccagnano, S.; Zakharov, L. N.; Rheingold, A. L.; Christou, G.; Hendrickson, D. N. *Polyhedron* **2003**, *22* (14−17), 1727−1733.
(31) del Barco, E.; Kent, A. D.; Yang, E. C.; Hendrickson, D. N. *Phys. Rev. Lett.* **2004**, *93* (15), 157202/1−157202/4.
(32) Kuhler, T. C.; Swanson, M.; Shcherbuchin, V.; Larsson, H.; Mellgard, B.; Sjostrom, J. E. *J. Med. Chem.* **1998**, *41* (11), 1777−1788.

Table 1. Crystallographic Data for Complexes **1** and **2**

complex	**1**	**2**
formula	$C_{28}H_{42}Cl_4N_4Ni_4O_9$	$C_{32}H_{50}Cl_4N_4Ni_4O_9$
fw, g/mol	955.30	1011.40
temperature, K	173(2)	150(2)
space group	$I\bar{4}2d$	$I\bar{4}2d$
a, Å	16.1421(6)	16.6017(5)
b, Å	16.1421(6)	16.6017(5)
c, Å	29.4689(14)	29.3656(17)
α, deg	90	90
β, deg	90	90
γ, deg	90	90
volume, Å^3	7678.6(5)	8093.6(6)
Z, *Z*′	8, 0.5	8, 0.5
F(000)	3920	4176
density (calcd) g/cm^3	1.653	1.660
absorption coefficient, mm^{-1}	2.262	2.150
absorption correction	SADABS	SADABS
transmission max/min	0.714/0.660	0.739/0.565
reflns, measured	17832	25077
reflns, independent	4394 (R_{int} = 0.0451)	4845 (R_{int} = 0.0330)
reflns, observed	3949	4668
data/restraints/params	4394/1/231	4845/2/231
goodness-of-fit on F^2	1.120	1.107
R indices [$I > 2\sigma(I)$][a,b]	R = 0.0521	R = 0.0382
	$R(\omega F^2)$ = 0.1055	$R(\omega F^2)$ = 0.1049
R indices (all data)[a,b]	R = 0.0626	R = 0.0400
	$R(\omega F^2)$ = 0.1124	$R(\omega F^2)$ = 0.1069

[a] $R = \sum||F_o| - |F_c||/\sum|F_o|$. [b] $R(\omega F^2) = \{\sum[\omega(F_o^2 - F_c^2)^2]/\sum[\omega(F_o^2)^2]\}^{1/2}$; $\omega = 1/[\sigma^2(F_o^2) + (aP)^2 + bP]$, where $P = [2F_c^2 + \max(F_o,0)]/3$.

Table 2. Crystallographic Data for Complexes **3** and **4**

complex	**3**	**4**
formula	$C_{48}H_{80}Cl_4N_4Ni_4O_8$	$C_{60}H_{96}Cl_4N_4Ni_4O_8$
fw, g/mol	1217.80	1378.05
temperature, K	173(2)	150(2)
space group	$I4_1/a$	$C2/c$
a, Å	12.8389(3)	25.2519(16)
b, Å	12.8389(3)	20.2768(13)
c, Å	35.047(2)	40.811(3)
α, deg	90	90
β, deg	90	106.9140(10)
γ, deg	90	90
volume, Å^3	5777.1(4)	19993(2)
Z, *Z*′	4, 0.25	12, 1.5
F(000)	2560	8736
density (calcd), g/cm^3	1.400	1.373
absorption coefficient, mm^{-1}	1.519	1.325
absorption correction	SADABS	SADABS
transmission max/min	1.000/0.827	1.000/0.863
reflns, measured	18178	61994
reflns, independent	3323 (R_{int} = 0.0310)	22832 (R_{int} = 0.0335)
reflns, observed	3043	16942
data/restraints/params	3323/0/234	22832/0/1074
goodness-of-fit on F^2	1.268	1.002
R indices [$I > 2\sigma(I)$][a,b]	R = 0.0329	R = 0.0539
	$R(\omega F^2)$ = 0.0794	$R(\omega F^2)$ = 0.1279
R indices (all data)[a,b]	R = 0.0370	R = 0.0773
	$R(\omega F^2)$ = 0.0809	$R(\omega F^2)$ = 0.1405

[a] $R = \sum||F_o| - |F_c||/\sum|F_o|$. [b] $R(\omega F^2) = \{\sum[\omega(F_o^2 - F_c^2)^2]/\sum[\omega(F_o^2)^2]\}^{1/2}$; $\omega = 1/[\sigma^2(F_o^2) + (aP)^2 + bP]$, where $P = [2F_c^2 + \max(F_o,0)]/3$.

crystal was placed onto the array, and the external magnetic field was oriented to be parallel to the crystal easy axis.

Results and Discussion

Strategy. The goal of this work was to vary the electronic insulation between the Ni^{II}_4 complexes in the crystals of [Ni(hmp)(ROH)X]$_4$ (X^-= Cl^- or Br^-) in order to change the magnitude of the weak intermolecular magnetic exchange interactions. It was found that this could be achieved by dissolving the parent MeOH complex **1** (R = CH_3) in a solution of dichloromethane/ROH. After slow evaporation of this solution, crystalline samples of the complexes **2** (EtOH), **3** (3,3-dimethyl-1-butanol), and **4** (3-cyclohexyl-1-propanol) were isolated. The bromide complex **5** and the *tert*-butyl-substituted hmp^- complex **6** were also prepared according to a similar procedure. In the series of complexes **1**−**3**, the *tert*-butyl substituent on the alcohol ligand should provide the greatest insulation between complexes. In complex **6**, there are *tert*-butyl substituents on both the alcohol and the hmp^- ligand, and this should provide the maximum shielding in all six complexes.

Because the results of this article involve complicated physical data, it is important to discuss the order of presentation of the data at the outset. Magnetization hysteresis data definitively establish that the six Ni_4 complexes presented in this paper are single-molecule magnets (SMMs). The major goal in this work was to investigate how very weak intermolecular magnetic exchange interactions between Ni_4 complexes affect the magnetization tunneling in individual Ni_4 complexes. The order of presentation of this paper is as follows: First, we describe the X-ray structures of the six Ni_4 complexes with an eye toward possible pathways that propagate intermolecular magnetic exchange interactions. Second, we present detailed magnetization versus magnetic field data for single crystals that definitively establish these six Ni_4 complexes as SMMs. Third, we present dc magnetic susceptibility used to evaluate the ground-state spin *S* and axial zero-field splitting ($D\hat{S}_z^2$) for the six complexes. Fourth, we present variable-temperature ac magnetic susceptibility data. These Ni_4 SMMs do *not* exhibit frequency-dependent

Table 3. Crystallographic Data for Complexes **5** and **6**

complex	**5**	**6**
formula	$C_{48}H_{80}BrI_4N_4Ni_4O_8$	$C_{64}H_{112}Cl_4N_4Ni_4O_8$
fw, g/mol	1395.64	1442.22
temperature, K	213(2)	213(2)
space group	$I4_1/a$	$I\bar{4}2d$
a, Å	12.8739(3)	13.4080(4)
b, Å	12.8739(3)	13.4080(4)
c, Å	36.3672(19)	42.329(3)
α, deg	90	90
β, deg	90	90
γ, deg	90	90
volume, Å^3	6027.4(4)	7609.7(6)
Z, *Z*′	4, 0.25	4, 0.25
F(000)	2848	3072
density (calcd), g/cm^3	1.538	1.259
absorption coefficient, mm^{-1}	3.930	1.164
absorption correction	SADABS	SADABS
transmission max/min	1.000/0.729	1.000/0.785
reflns, measured	23208	27031
reflns, independent	3648 (R_{int} = 0.0280)	4469 (R_{int} = 0.0347)
reflns, observed	2966	3918
data/restraints/params	3648/0/234	4469/18/183
goodness-of-fit on F^2	1.027	1.148
R indices [$I > 2\sigma(I)$][a,b]	R = 0.0256	R = 0.0506
	$R(\omega F^2)$ = 0.0646	$R(\omega F^2)$ = 0.1343
R indices (all data)[a,b]	R = 0.0358	R = 0.0575
	$R(\omega F^2)$ = 0.0686	$R(\omega F^2)$ = 0.1395

[a] $R = \sum||F_o| - |F_c||/\sum|F_o|$. [b] $R(\omega F^2) = \{\sum[\omega(F_o^2 - F_c^2)^2]/\sum[\omega(F_o^2)^2]\}^{1/2}$; $\omega = 1/[\sigma^2(F_o^2) + (aP)^2 + bP]$, where $P = [2F_c^2 + \max(F_o,0)]/3$

(33) Wernsdorfer, W. *Adv. Chem. Phys.* **2001**, *118*, 99−190.

out-of-phase ac signals as seen for many other SMMs. The in-phase ac signal disappears, and an out-of-phase ac signal is observed. The kinetics sensed by these ac signals is not simply due to an isolated Ni_4 SMM. The Ni_4 complexes do not magnetically order, as the Ni_4 complexes continue to exhibit magnetization tunneling at temperatures below the temperatures at which the ac signals change. The in-phase ac signal disappears at low temperatures because the same numbers of Ni_4 complexes always tunnel forward and backward.

X-ray Structures of Complexes 1 and 2. The MeOH (**1**) and EtOH (**2**) complexes are isostructural and crystallize in the $I\bar{4}2d$ space group. Table 1 gives the details of the crystallography for these two complexes. All six of the complexes with the composition $[Ni(hmp)(ROH)X]_4$ have a distorted metal-oxide cubane core with four Ni(II) ions and four oxygen atoms of the four hmp^- ligands occupying alternating corners. Each Ni(II) ion is chelated by an hmp^- ligand and is also coordinated by a halide ion, an oxygen atom from the alcohol (ROH) ligand, and three oxygen atoms from three other hmp^- ligands. Thus, each Ni(II) ion is six-coordinate, and except for complex **4**, all Ni_4 molecules have S_4 site symmetry.

Both complexes **1** and **2** contain two symmetrically independent $[Ni(hmp)(ROH)Cl]_4$ complexes: one in a general position and the other on an inversion axis. The differences in the bond distances and angles for the two different Ni_4 complexes in both **1** and **2** are relatively small (Table 4). It should be noted that the dimensions in all six Ni_4 complexes **1**−**6** reported in this work are quite similar. The ethyl arms of the EtOH ligands in **2** are disordered over two positions in a ratio of 7:2 (Figure 2 below).

In all six complexes **1**−**6**, there are intramolecular O−H···Hal (Hal = Cl, Br) hydrogen bonds. The protons from the OH group of the alcoholic ligand in **1** and **2** interact with the nearby chloride ligand to form relatively strong intramolecular hydrogen bonds (Figure 1 shows complex **1**; a drawing of complex **2** is given in the Supporting Information). The distances for the two different Ni_4 molecules in complex **1** are 3.026(6) and 3.043(5) Å for O···Cl contacts and 2.2(1) and 2.22(7) Å for the H···Cl contacts. The H atoms were located by residual electron density. It has been reported[34] that a H···Cl contact can be classified as "short" for a distance of less than 2.52 Å, "intermediate" in the range of 2.52−2.95 Å, and "long" in the range of 2.95−3.15 Å. The intramolecular hydrogen bonds in complex **1** fall into the short category and thus involve relatively strong intramolecular hydrogen bonds. The H atom involved in the hydrogen bond was not found from the real *F* map for complex **2**, but the O···Cl distances in **2**, 3.038(3) and 3.024(3) Å, are close to those in **1** and also indicate the presence of strong hydrogen bonds. These hydrogen bonds restrict the freedom of the MeOH ligand from rotating about the Ni−O bonds to some degree. The H atoms involved in the O−H···Cl hydrogen bonds are slightly out of the average plane of the NiOClNi fragment. A disorder of the ROH groups over two positions seems to be related to two possible positions of the H atoms involved in such hydrogen bonds: up and down relative to the average plane.

Table 4. Metal−Ligand Bond Lengths (Å) and Angles (deg) in Complexes **1** and **2**

Complex **1**[a]			
Ni(1)−O(1)	2.049(4)	O(3)#3−Ni(2)−N(2)	160.68(17)
Ni(1)−O(1)#1	2.067(4)	O(3)−Ni(2)−O(3)#4	80.76(15)
Ni(1)−N(1)	2.080(4)	O(3)#3−Ni(2)−O(3)#4	80.87(14)
Ni(1)−O(1)#2	2.105(4)	N(2)−Ni(2)−O(3)#4	101.51(18)
Ni(1)−O(2)	2.111(5)	O(3)−Ni(2)−O(4)	94.19(18)
Ni(1)−Cl(1)	2.3677(17)	O(3)#3−Ni(2)−O(4)	86.19(16)
Ni(2)−O(3)	2.046(4)	N(2)−Ni(2)−O(4)	89.63(19)
Ni(2)−O(3)#3	2.052(3)	O(3)#4−Ni(2)−O(4)	166.64(15)
Ni(2)−N(2)	2.068(4)	O(3)−Ni(2)−Cl(2)	174.95(12)
Ni(2)−O(3)#4	2.087(4)	O(3)#3−Ni(2)−Cl(2)	99.22(11)
Ni(2)−O(4)	2.098(4)	N(2)−Ni(2)−Cl(2)	99.70(15)
Ni(2)−Cl(2)	2.3716(16)	O(3)#4−Ni(2)−Cl(2)	94.51(11)
O(1)−Ni(1)−O(1)#1	82.20(17)	O(4)−Ni(2)−Cl(2)	90.81(15)
O(1)−Ni(1)−N(1)	79.79(17)	C(12)−N(2)−Ni(2)	128.6(4)
O(1)#1−Ni(1)−N(1)	161.27(18)	C(8)−N(2)−Ni(2)	111.9(4)
O(1)−Ni(1)−O(1)#2	79.69(17)	C(6)−O(1)−Ni(1)	110.4(3)
O(1)#1−Ni(1)−O(1)#2	80.87(16)	C(6)−O(1)−Ni(1)#5	127.5(4)
N(1)−Ni(1)−O(1)#2	100.82(18)	Ni(1)−O(1)−Ni(1)#5	98.43(17)
O(1)−Ni(1)−O(2)	91.6(2)	C(6)−O(1)−Ni(1)#2	119.0(4)
O(1)#1−Ni(1)−O(2)	89.44(17)	Ni(1)−O(1)−Ni(1)#2	100.00(17)
N(1)−Ni(1)−O(2)	85.97(19)	Ni(1)#5−O(1)−Ni(1)#2	96.67(16)
O(1)#2−Ni(1)−O(2)	167.73(17)	C(7)−O(2)−Ni(1)	132.6(10)
O(1)−Ni(1)−Cl(1)	173.87(13)	C(13)−O(3)−Ni(2)	110.0(3)
O(1)#1−Ni(1)−Cl(1)	99.72(12)	C(13)−O(3)−Ni(2)#6	126.5(3)
N(1)−Ni(1)−Cl(1)	98.72(14)	Ni(2)−O(3)−Ni(2)#6	98.58(15)
O(1)#2−Ni(1)−Cl(1)	94.81(12)	C(13)−O(3)−Ni(2)#4	120.6(3)
O(2)−Ni(1)−Cl(1)	94.23(16)	Ni(2)−O(3)−Ni(2)#4	98.74(15)
O(3)−Ni(2)−O(3)#3	81.86(15)	Ni(2)#6−O(3)−Ni(2)#4	97.25(15)
O(3)−Ni(2)−N(2)	79.64(17)	C(14)−O(4)−Ni(2)	130.6(5)
Complex **2**[b]			
Ni(1)−O(1)	2.045(2)	Ni(1)#3−O(1)−Ni(1)#2	97.07(10)
Ni(1)−O(1)#1	2.052(2)	C(7A)−O(2)−C(7)	46.0(8)
Ni(1)−N(1)	2.057(3)	C(7A)−O(2)−Ni(1)	133.9(7)
Ni(1)−O(1)#2	2.093(3)	C(7)−O(2)−Ni(1)	125.8(3)
Ni(1)−O(2)	2.105(3)	C(1)−N(1)−C(5)	118.7(3)
Ni(1)−Cl(1)	2.3789(10)	C(1)−N(1)−Ni(1)	128.8(3)
Ni(1′)−O(1′)	2.044(3)	C(5)−N(1)−Ni(1)	112.2(2)
Ni(1′)−O(1′)#4	2.058(2)	O(1′)−Ni(1′)−O(1′)#4	82.27(11)
Ni(1′)−N(1′)	2.058(3)	O(1′)−Ni(1′)−N(1′)	80.44(12)
Ni(1′)−O(1′)#5	2.103(3)	O(1′)#4−Ni(1′)−N(1′)	162.06(12)
Ni(1′)−O(2′)	2.113(3)	O(1′)−Ni(1′)−O(1′)#5	79.27(11)
Ni(1′)−Cl(1′)	2.3740(10)	O(1′)#4−Ni(1′)−O(1′)#5	80.86(11)
O(1)−Ni(1)−O(1)#1	81.95(10)	N(1′)−Ni(1′)−O(1′)#5	100.47(11)
O(1)−Ni(1)−N(1)	79.96(11)	O(1′)−Ni(1′)−O(2′)	91.82(12)
O(1)#1−Ni(1)−N(1)	161.11(12)	O(1′)#4−Ni(1′)−O(2′)	89.74(11)
O(1)−Ni(1)−O(1)#2	80.38(10)	N(1′)−Ni(1′)−O(2′)	86.09(12)
O(1)#1−Ni(1)−O(1)#2	80.81(10)	O(1′)#5−Ni(1′)−O(2′)	167.79(11)
N(1)−Ni(1)−O(1)#2	101.37(11)	O(1′)−Ni(1′)−Cl(1′)	174.78(8)
O(1)−Ni(1)−O(2)	93.20(12)	O(1′)#4−Ni(1′)−Cl(1′)	99.20(8)
O(1)#1−Ni(1)−O(2)	86.82(10)	N(1′)−Ni(1′)−Cl(1′)	98.44(9)
N(1)−Ni(1)−O(2)	88.80(12)	O(1′)#5−Ni(1′)−Cl(1′)	95.98(8)
O(1)#2−Ni(1)−O(2)	166.73(10)	O(2′)−Ni(1′)−Cl(1′)	93.19(10)
O(1)−Ni(1)−Cl(1)	175.31(8)	C(6′)−O(1′)−Ni(1′)	109.8(2)
O(1)#1−Ni(1)−Cl(1)	99.26(8)	C(6′)−O(1′)−Ni(1′)#6	128.4(2)
N(1)−Ni(1)−Cl(1)	99.21(10)	Ni(1′)−O(1′)−Ni(1′)#6	98.37(11)
O(1)#2−Ni(1)−Cl(1)	95.30(7)	C(6′)−O(1′)−Ni(1′)#5	118.5(2)
O(2)−Ni(1)−Cl(1)	91.40(9)	Ni(1′)−O(1′)−Ni(1′)#5	100.48(11)
C(6)−O(1)−Ni(1)	110.1(2)	Ni(1′)#6−O(1′)−Ni(1′)#5	96.51(10)
C(6)−O(1)−Ni(1)#3	127.3(2)	C(7′)−O(2′)−Ni(1′)	134.7(13)
Ni(1)−O(1)−Ni(1)#3	98.59(10)	C(5′)−N(1′)−C(1′)	118.8(3)
C(6)−O(1)−Ni(1)#2	119.6(2)	C(5′)−N(1′)−Ni(1′)	112.3(2)
Ni(1)−O(1)−Ni(1)#2	99.19(10)	C(1′)−N(1′)−Ni(1′)	128.5(3)

[a] Symmetry transformations used to generate equivalent atoms for complex 1: #1 $y + 1/2$, $-x + 3/2$, $-z + 1/2$; #2 $-x + 2$, $-y + 1$, z; #3 y, $-x + 1$, $-z$; #4 $-x + 1$, $-y + 1$, z; #5 $-y + 3/2$, $x - 1/2$, $-z + 1/2$; #6 $-y + 1$, x, $-z$; #7 $x + 0$, $-y + 3/2$, $-z + 1/4$. [b] Symmetry transformations used to generate equivalent atoms for complex 2: #1 $y + 1/2$, $-x - 1/2$, $-z + 3/2$; #2 $-x$, $-y - 1$, z; #3 $-y - 1/2$, $x - 1/2$, $-z + 3/2$; #4 $-y + 1/2$, $x - 1/2$, $-z + 3/2$; #5 $-x + 1$, $-y$, z; #6 $y + 1/2$, $-x + 1/2$, $-z + 3/2$; #7 $x + 0$, $-y - 1/2$, $-z + 5/4$.

(34) Aullon, G.; Bellamy, D.; Brammer, L.; Bruton, E. A.; Orpen, A. G. *Chem. Commun.* **1998**, (6), 653−654.

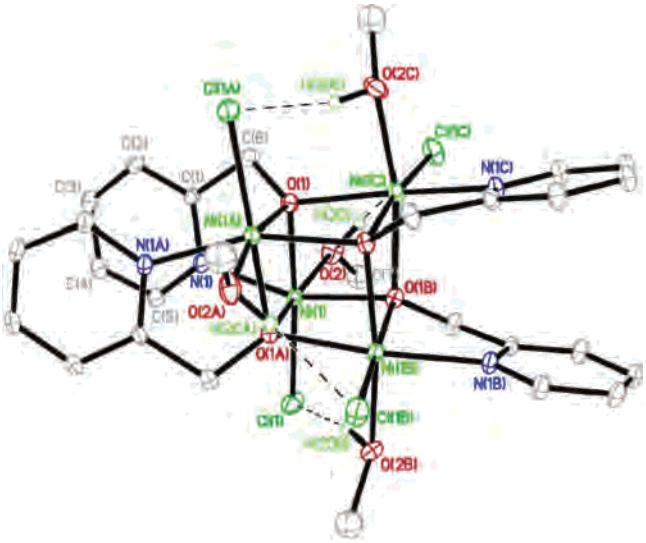

Figure 1. 30% ORTEP plot of complex 1, $[Ni(hmp)(MeOH)Cl]_4$.

Because we are interested in the effects of intermolecular interactions on the quantum tunneling of magnetization, it is important to investigate the packing in the crystals of complexes **1** and **2**, looking closely at the intermolecular contacts that could affect magnetic exchange interactions between Ni_4 molecules. For both complexes **1** and **2**, there are two symmetrically independent Ni_4 molecules, one sitting at the body center and the other at the C-face center. Each $[Ni(hmp)(ROH)Cl]_4$ molecule is surrounded tetrahedrally by four other Ni_4 molecules. Thus, the body-centered Ni_4 molecule forms one diamond-like lattice, and the Ni_4 molecule that is at the C-face center forms a second diamond-like lattice. These two interpenetrating diamond-like lattices are illustrated in Figure 2 for complex **1**. In the crystal lattices of complexes **1** and **2**, there is also a H_2O solvate molecule that is not fully occupied and also is disordered. The distances from the oxygen atom of the solvate water molecule to the Cl^- ligand are in the range of 3.6−3.8 Å for complex **1** and 3.97 Å for complex **2**. This could lead to weak hydrogen-bonding interactions. Because the H_2O solvate molecules are disordered and because there are two crystallographically different Ni_4 molecules in complex **1** (also in complex **2**), this could lead to range of microenvironments, that is, Ni_4 molecules that experience different crystal environments. The explanation for the symmetry of QTM in Mn_{12}–Ac involved six different microenvironments present for Mn_{12} molecules as a result of disordered solvate molecules in the crystal, and this was confirmed by precise HFEPR spectroscopy and micro-Hall magnetometry.[24,26,35]

In a recent report,[29] it was shown that intermolecular C−H···Cl hydrogen bonds and Cl···Cl contacts provide a pathway for intermolecular magnetic exchange interactions between two $S = {}^9/_2$ Mn_4 SMMs. This type of hydrogen bond is also observed in this Ni_4 series of complexes. Chloride ligands from one Ni_4 molecule interact with certain hydrogen atoms from the pyridine moiety of the hmp^- ligand on a neighboring Ni_4 molecule. In the cases of complexes **1** and **2**, chloride ions contact with the hydrogen atoms at the 5 and 6 positions of the hmp^- pyridine ring. The Cl···H distances are 2.9 and 3.0 Å in complex **1** and 3.0 Å in complex **2**. These distances are only slightly longer than the reported literature value of 2.8 Å.[29] Hence, intermolecular magnetic exchange interactions through this pathway could lead to an exchange bias seen in magnetization hysteresis loops.

Another possible pathway for intermolecular magnetic exchange interactions involves the Cl···Cl contacts between Ni_4 molecules. The shortest Cl···Cl contacts are 4.867 and 4.862 Å in complex **1** and 4.951 and 4.884 Å in complex **2** for the molecules on the body and at the C-face centers, respectively. In both complexes, the Cl···Cl distances are significantly longer than the sum of the van der Waals radii of two chloride ions, 3.6 Å;[29,36] thus, the intermolecular Cl···Cl contacts in both complexes **1** and **2** are long and likely do not lead to intermolecular magnetic exchange interactions. In summary, two different types of intermolecular contacts are present in complexes **1** and **2** that could lead to magnetic exchange interactions between Ni_4 molecules. One contact involves the H_2O solvate molecule. The other involves a Cl···H−C (pyridine) contact. Although it is not possible to anticipate whether the observed contacts would lead to intermolecular antiferromagnetic or ferromagnetic exchange interactions, it is possible to predict that complex **1** would exhibit a stronger interaction than complex **2**.

X-ray Structure of Complex 3. Complex **3** crystallizes in the tetragonal space group $I4_1/a$. As with complexes **1** and **2**, complex **3** has a distorted cubane core with S_4 symmetry; however, the alcohol ligands in the complex **3** have a longer aliphatic chain (figure available in Supporting Information). There is only one symmetrically independent molecule in the unit cell. An examination of the conformation of the aliphatic chain in the dmb ligand by a Newman projection viewed along the C7−C8 bond shows that the substituents are in a staggered conformation with the *tert*-butyl substituent in a trans position relative to the OH group as well as the main body of the complex. The molecule adopts this conformation to avoid having the bulky *tert*-butyl group approach the main body of the complex. On the other hand, because there is less restriction for the *tert*-butyl rotating about the C8−C9 bond, the thermal parameters for the C10−C12 atoms are considerably larger than those for all of the other carbon atoms. The coordinates and the thermal parameters of complex **3** are listed in Table 5.

No packing solvate or water molecules are found in the crystal lattice of complex **3**. Hence, intermolecular interactions between the metal complex and lattice solvate molecules is not an issue in this compound. Recently, it was reported that the lattice solvate molecule can have a profound influence on the QTM in Mn_{12} SMMs.[35,37] The absence of

(35) Cornia, A.; Sessoli, R.; Sorace, L.; Gatteschi, D.; Barra, A. L.; Daiguebonne, C. *Phys. Rev. Lett.* **2002**, *89* (25), 257201.

(36) Freytag, M.; Jones, P. G.; Ahrens, B.; Fischer, A. K. *New J. Chem.* **1999**, *23* (12), 1137−1139.

(37) Cornia, A.; Fabretti, A. C.; Sessoli, R.; Sorace, L.; Gatteschi, D.; Barra, A. L.; Daiguebonne, C.; Roisnel, T. *Acta Crystallogr. C* **2002**, *58*, m371−m373.

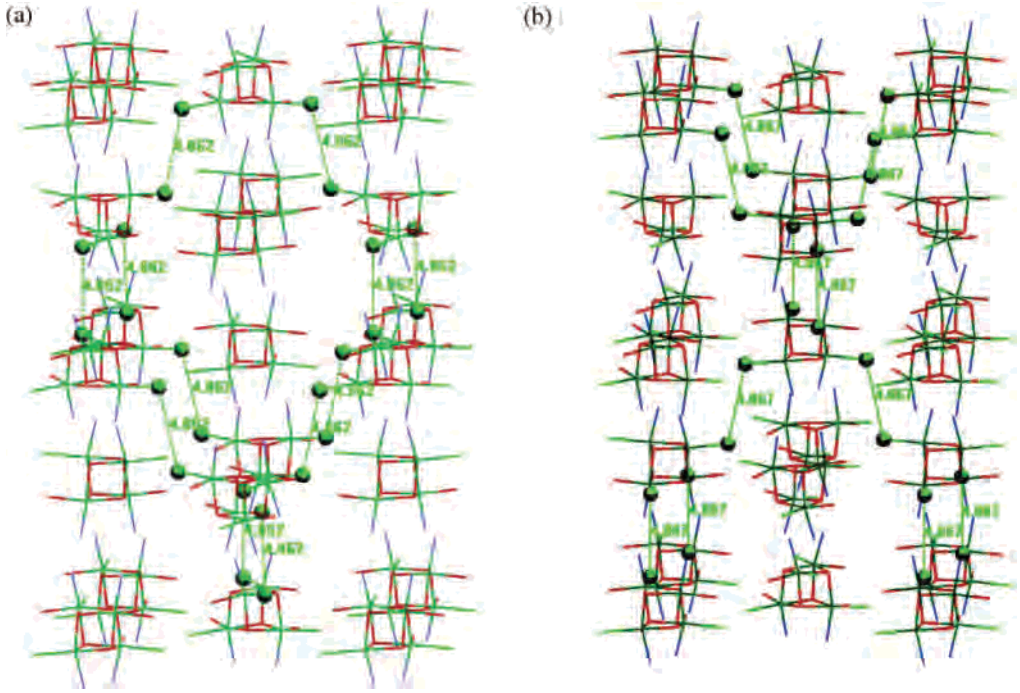

Figure 2. Illustration of the interpenetrating diamond-like sublattices of complex **1**, where green balls represent the chlorides. All carbon and hydrogen atoms are omitted for clarity, and the two plots represent (a) the sublattice linked from the C-face center, (b) the sublattice linked from body center.

Table 5. Atomic Coordinates ($\times 10^4$) and Equivalent Isotropic Displacement Parameters ($Å^2 \times 10^3$) for Complex **3**[a]

	x	*y*	*z*	*U*(eq)[a]
Ni(1)	791(1)	3443(1)	943(1)	15(1)
Cl(1)	634(1)	5262(1)	867(1)	22(1)
O(1)	816(1)	1859(1)	976(1)	16(1)
O(2)	2384(1)	3581(1)	1053(1)	22(1)
N(1)	1110(1)	3075(1)	382(1)	17(1)
C(1)	1047(2)	3684(2)	71(1)	21(1)
C(2)	1343(2)	3349(2)	−289(1)	26(1)
C(3)	1733(2)	2349(2)	−327(1)	26(1)
C(4)	1799(2)	1720(2)	−9(1)	22(1)
C(5)	1474(1)	2097(1)	343(1)	18(1)
C(6)	1501(2)	1446(2)	701(1)	19(1)
C(7)	3174(2)	3955(2)	800(1)	24(1)
C(8)	4109(2)	4347(2)	1020(1)	22(1)
C(9)	4986(2)	4814(2)	774(1)	31(1)
C(10)	4564(2)	5656(3)	511(1)	49(1)
C(11)	5515(2)	3953(3)	545(1)	48(1)
C(12)	5795(2)	5295(2)	1040(1)	42(1)

[a] *U*(eq) is defined as one-third of the trace of the orthogonalized U_{ij} tensor.

lattice solvate molecules in complex **3** makes it a relatively "clean" candidate for the study of QTM. The shortest Cl···Cl contacts between neighbor molecules in compound **3** are about 6.036 and 6.408 Å, which are far longer than the 3.6 Å obtained for the sum of the van der Waals radii of two chloride ions. Therefore, intermolecular magnetic exchange interactions propagated by this pathway should be negligible. Although a bulky aliphatic group is incorporated on the dbm alcohol ligand, intermolecular hydrogen bonds between chloride ligands on one complex and a hydrogen atom from the pyridine of hmp^- ligands on a neighboring complex are still observed in complex **3**. In this case, the chloride ligands approach two pyridines of the hmp^- ligands of a neighboring molecule with distances 3.031 Å to the hydrogen at the 5 position on one hmp^- and 3.045 Å to the hydrogen at the 4 position of another hmp^-. These H···Cl distances in complex **3** are in the same range as found for complexes **1** and **2**. Thus, this could also be a factor affecting the magnitude of intermolecular magnetic exchange interactions in complex **3**. As with complexes **1** and **2**, it is not possible to conclude from the nature of Cl···H−C contacts in complex **3** whether the intermolecular exchange interactions would be expected to be antiferromagnetic or ferromagnetic.

Intramolecular hydrogen bonds from the protons on OH groups to the chloride ligands are also seen in complex **3** and can be classified as being in the short hydrogen-bond category based on the found H···Cl distance, 2.300 Å. This interaction also could restrict the aliphatic chain on the 3,3-dimethyl-1-butanol ligand from free rotation about the metal−oxygen bond.

X-ray Structure of Complex 4. In contrast to complexes **1**−**3**, complex **4** crystallizes in the monoclinic space group *C*2/*c*. Although complex **4** also has a distorted cubane core, it does not have S_4 site symmetry in the crystal. There are two crystallographically independent molecules in the crystal of **4**: one in a general position with C_1 site symmetry and the other in a special position with C_2 site symmetry. The fact that both of these molecules do not have S_4 site symmetry indicates that appreciable transverse zero-field interactions are likely to be present that would lead to even faster QTM than observed in complexes **1**−**3**.[38] The disorder of the aliphatic chain in complex **4** is more extensive than that in complex **3**. An ORTEP plot for

(38) Aliaga-Alcalde, N.; Edwards, R. S.; Hill, S. O.; Wernsdorfer, W.; Folting, K.; Christou, G. *J. Am. Chem. Soc.* **2004**, *126* (39), 12503−12516.

Table 6. Nonclassical Intermolecular Hydrogen-Bond Lengths (Å) in the Crystal of Complex **4**

C_1-symmetry molecule[a]			C_2-symmetry molecule[a]		
mol type (H on Py)[b]	Py → Cl[c]	Cl → Py[d]	mol type [b]	Py → Cl[c]	Cl → Py[d]
C_2 (3)	3.201	3.457	C_1 (3)	3.457	3.201
C_2 (4)	3.037	3.232	C_1 (4)	3.232	3.037
C_2 (3)	2.863	2.889	C_1 (3)	2.889	2.863
C_2 (4)	3.732	3.583	C_1 (4)	3.583	3.732
C_1 (3)	2.755	2.755	C_1 (3)	3.457	3.201
C_1 (4)	3.267	3.267	C_1 (4)	3.232	3.037
C_1 (3)	2.906	2.906	C_1 (3)	2.889	2.863
C_1 (4)	2.998	2.998	C_1 (4)	3.583	3.732

[a] Type of object molecule. [b] Symbols in columns 1 and 4 indicate the type of the neighboring molecule named by symmetry, with the position of H on the pyridine ring of hmp ligand in parentheses, e.g., C_2 (3) means the neighboring molecule has C_2 symmetry contact through the H atom on position 3 of the hmp ring. [c] Py → Cl: the hmp ligand is on the object molecule and chloride is on the neighboring molecule. [d] Cl → Py: the hmp ligand is on the neighboring molecule, and chloride is on the object molecule.

complex **4** given in the Supporting Information shows the disorder of the 3-cyclohexyl-1-propanol ligand. Once again, no crystal solvate molecule is found in the lattice of complex **4**; thus, intermolecular magnetic exchange interactions are not propagated by solvate molecules. Cl···Cl contacts in this complex are all in excess of 7 Å; therefore, magnetic exchange interactions propagated through this pathway would be much weaker than those in complex **3**. Intermolecular interactions between hydrogen atoms on the hmp^- ligand and chloride ligands on neighboring molecules are seen. Because of the low symmetry of this crystal, these H···Cl contact distances vary over a wide range. Most of these nonclassical hydrogen bonds are around 3 Å, some of them run to 3.76 Å, and a few of them are extremely short at 2.755 Å. Table 6 summarizes the nonclassical hydrogen bonds within the crystal lattice. Here, we classify the molecules according to their symmetry as C_1 and C_2 molecules. Each C_1 molecule contacts with both C_1 and C_2 molecules through the nonclassical hydrogen bonds but C_2 molecules make contact with C_1 molecules only through these nonclassical hydrogen bonds.

X-ray Structure of Complex 5. Complex **5** is an analogue of complex **3** in which the chloride ligands have been replaced by bromides (an ORTEP plot is available in the Supporting Information). The two complexes not only have the same packing and $I4_1/a$ space group, but also have the same S_4 site symmetry. The aliphatic chain of the 3,3-dimethyl-1-butanol ligand adopts the same conformation in complex **5** as in complex **3**, with the *tert*-butyl group directed away from the main body of the complex. No crystal solvate molecule is found in the lattice. The Br···Br contacts in complex **5** are 5.738 and 6.597 Å. One of them is longer than the corresponding Cl···Cl contact in complex **3**, but the shorter Br···Br contact in complex **5** is shorter than the Cl···Cl contact in complex **3**. These Br···Br distances are considerably larger than the sum of the van der Waals radii of two bromides, which is equal to 3.7 Å. Intermolecular H···Br hydrogen bonds involving hydrogen atoms on the hmp^- ligands are the same as in complex **3**, with H···Br distances of 3.106 Å for the hydrogen atom on the 4 position of one hmp^- ligand and 3.191 Å for the hydrogen on the 5 position of another hmp^-. Both are close to the sum of the van der Waals radii of hydrogen and bromide of 3.05 Å. Intramolecular hydrogen bonds in this complex are also seen with H···Br distances of 2.432 Å.

X-ray Structure of Complex 6. Complex **6** crystallizes in the $I\bar{4}2d$ space group, where each unit cell contains only one kind of crystallographically independent molecule with S_4 site symmetry. Because of the added bulk of the *tert*-butyl group on the hmp^- ligand, more free space is available in the crystal of complex **6**. As a consequence, the aliphatic chain of the 3,3-dimethyl-1-butanol (dmb) ligand on complex **6** exhibits greater disorder than does the same ligand in complex **3** (an ORTEP plot is available in the Supporting Information). The aliphatic chains are disordered for complex **6** and reside in two possible positions. The *tert*-butyl groups on both the *t*-Buhmp and 3,3-dimethyl-1-butanol ligands are highly disordered, as indicated by their large thermal parameters. The Cl···Cl contact distances seen in complex **6** are characterized by distances of 6.377 Å for the molecules on the same $a-b$ plane and 7.868 Å for the molecules on adjacent layers of the $a-c$ plane. These values are larger than those in complex **3** and are significantly larger than the sum of van der Waals radii of two chloride ions. Nonclassical intermolecular hydrogen bonds for chloride ions interacting with the hydrogen atoms on the 5 position of the hmp^- ligands in complex **6** are significantly weaker than those in all of the previous complexes, as evidenced by the Cl···H distance of 3.540 Å, which is significantly longer than those in complexes **1**−**4**, where 2.9−3.2 Å distances are found as compared to the sum of van der Waals radii of 2.95 Å. Intramolecular hydrogen bonds between the chlorides and the protons on alcohol ligand have H···Cl distances of 2.448 Å. Although they still fall in the short contact category, this value is somewhat longer than those in complexes **1**−**3**.

Some conclusions can be drawn from the above structural information about intermolecular contacts observed for complexes **1**−**6**. First, the *tert*-butyl groups on the two different ligands in complex **6** clearly lead to the greatest insulation between Ni_4 complexes of all six complexes. Intermolecular magnetic exchange interactions would be anticipated to be the weakest for complex **6**. Second, for the two isostructural complexes **1** and **2**, intermolecular exchange interactions should be greater for complex **1**. Third, complex **3** would be expected to exhibit weaker intermolecular magnetic exchange interactions than complexes **1** and **2**. Fourth, it is difficult to determine whether observed intermolecular contacts would lead to either net antiferromagnetic or ferromagnetic ordering. Fifth, because of the Br^- ligand in complex **5** and the low site symmetries in complex **4**, it is difficult to anticipate the nature of the intermolecular exchange interactions in these two complexes.

Magnetization versus Magnetic Field Hysteresis Loops. To examine how the chemical tuning of the peripheral ligands in the $[Ni(hmp)(ROH)X]_4$ complexes affects the magnetic properties of the complex, magnetization versus

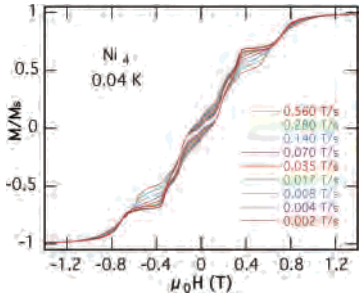

Figure 3. Magnetization hysteresis loops of a single crystal of [Ni(hmp)(MeOH)Cl]$_4$ (**1**) at 0.04 K at various scan rates from 0.002 to 0.56 T/s. The external magnetic field is oriented parallel to the easy axis of the crystal. Magnetization is plotted as a fraction of the maximum value of M_s, the saturation magnetization.

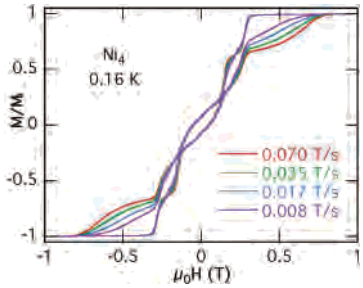

Figure 4. Hysteresis loops of a single-crystal sample of [Ni(hmp)(EtOH)Cl]$_4$ (**2**) at 0.16 K at various scan rates from 0.008 to 0.07 T/s. The magnetic field is oriented parallel to the easy axis of the crystal. Magnetization is plotted as a fraction of the maximum value of M_s, the saturation magnetization.

magnetic field hysteresis measurements were carried out for single crystals of complexes **1**−**6**. Magnetization hysteresis data were obtained for each of the six complexes with a micro-SQUID array in the range of 0.040−6.0 K at scan rates of 0.002−0.56 T/s. The field was aligned parallel to the mean easy axis of magnetization using the transverse field method.[39] Hysteresis is seen for all six complexes, and it is concluded that complexes **1**−**6** are single-molecule magnets (see Figures 3−8). For a single crystal of an SMM that has negligible intermolecular exchange interactions, the first step in the hysteresis loop due to quantum tunneling occurs at zero field when the external field is oriented parallel to the easy axis of the crystal. In a recent report,[29] it has been found that the presence of intermolecular exchange interactions in the supramolecular dimer $[Mn_4O_3Cl_4(O_2CEt)_3(py)_3]_2$ shifts the first step to a nonzero magnetic field. The $[Mn_4]$ units in the dimer interact with each other through six C−H···Cl hydrogen bonds and one Cl···Cl contact. These contacts within the $[Mn_4]_2$ dimer lead to a weak intermolecular antiferromagnetic interaction ($J = -0.05$ K for $H = -2JS_1 \cdot S_2$) between the two $S = {}^9/_2$ SMMs.[29,40] This antiferromagnetic interaction shifts the first hysteresis step significantly from zero field to −0.33 T.

The hysteresis loops of complexes **1** and **2** are illustrated in Figures 3 and 4. The first steps for both complexes are shifted from zero field. Obviously, there are intermolecular antiferromagnetic exchange interactions between neighboring molecules. The first step of the hysteresis loop is shifted to −0.33 T for complex **1** and to −0.28 T for complex **2**, indicating that the intermolecular interactions are stronger in complex **1** than in complex **2**. This results from the fact that complex **1** has shorter distances associated with the two significant intermolecular contacts: (i) hydrogen bonding between the crystal water molecules and chloride ligands and (ii) nonclassical hydrogen bonding between hydrogen atoms on the hmp^- ligands of one Ni_4 complex and the chloride ligands of a neighboring Ni_4 complex.

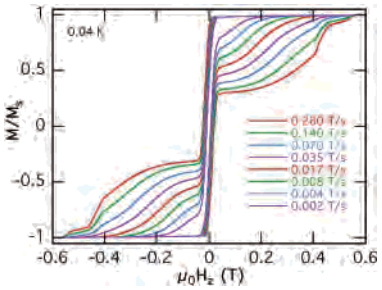

Figure 5. Magnetization hysteresis loops of a single crystal of [Ni(hmp)(dmb)Cl]$_4$ (**3**) measured at scan rates ranging from 0.002 to 0.280 T/s at 0.04 K. Magnetization is plotted as a fraction of the maximum value of M_s, the saturation magnetization.

Figure 5 illustrates the hysteresis loops for [Ni(hmp)(dmb)Cl]$_4$ (**3**). Because a bulky aliphatic chain on the dmb ligand has been incorporated, the Ni_4 molecules are more isolated from each other, which should reduce the intermolecular magnetic dipolar and magnetic exchange interactions. There are also no solvate molecules in the crystal of complex **3**. Although the intermolecular nonclassical hydrogen bonds present in complex **3** are of the same magnitude as those in complexes **1** and **2**, the intermolecular Cl···Cl contact distances are significantly longer in complex **3**. With all of the comparisons given above, the first step feature in the hysteresis loop due to the ground-state QTM in complex **3** should be shifted closer to zero magnetic field. Indeed, in Figure 5, it is observed that the ground-state QTM occurs essentially at zero field. The fact that the first step is sharp indicates that there is a relatively high rate of magnetization quantum tunneling in complex **3**. A detailed analysis of the magnetization hysteresis loop for complex **3** is presented in the next section.

Hysteresis loops for [Ni(hmp)(chp)Cl]$_4$ (**4**) are shown in Figure 6. As with complex **3**, no solvate molecules are found in the crystal of complex **4**. Although some of the nonclassical H···Cl contacts in complex **4** are even shorter than those observed in complexes **1**−**3**, the intermolecular Cl···Cl contact distances are larger than those in complex **3**. As a consequence of these observations, it is reasonable to anticipate that the first step of the hysteresis loop for complex **4** will occur close to zero field. This is confirmed by the experimental results, as shown in Figure 6. Detailed study of the hysteresis loops also shows that the step around zero field is actually split into two parts: one is above zero field, and the other is below zero field. This feature provides a clear indication of a small exchange bias caused by intermolecular antiferromagnetic interactions.

(39) Wernsdorfer, W.; Chakov, N. E.; Chirstou, G. *Phys. Rev. B* **2004**, *70*, 132413.
(40) Hill, S.; Edwards, R. S.; Aliaga-Alcalde, N.; Christou, G. *Science* **2003**, *302* (5647), 1015−1018.

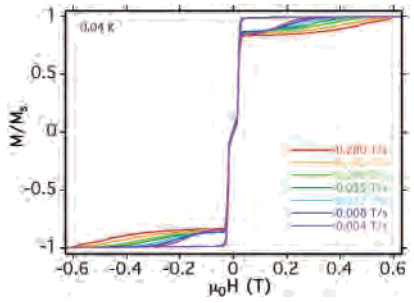

Figure 6. Magnetization hysteresis loops of a single crystal of [Ni(hmp)(chp)Cl]$_4$ (**4**) at 0.04 K at various scan rates from 0.004 to 0.28 T/s. The magnetic field is parallel to the easy axis. The magnetization is plotted as a fraction of the maximum value of M_s, the saturation magnetization.

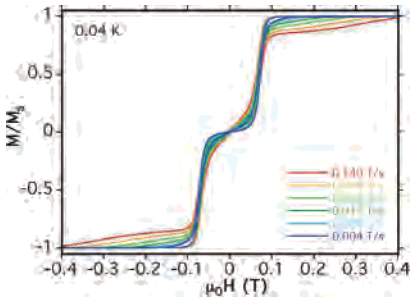

Figure 7. Magnetization hysteresis loops of a single crystal of [Ni(hmp)(dmb)Br]$_4$ (**5**) at 0.04 K at various scan rates from 0.004 to 0.14 T/s. The magnetic field is parallel to the easy axis. The magnetization is plotted as a fraction of the maximum value of M_s, the saturation magnetization.

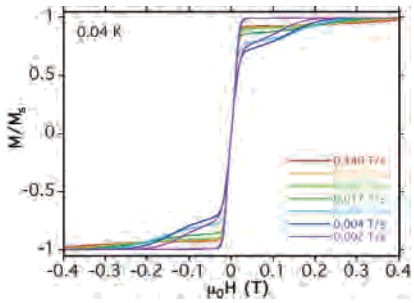

Figure 8. Magnetization hysteresis loops of a single crystal of [Ni(*t*-Buhmp)(dmb)Cl]$_4$ (**6**) at 0.04 K at various scan rates from 0.004 to 0.14 T/s. The magnetic field is parallel to the easy axis. The magnetization is plotted as a fraction of the maximum value of M_s, the saturation magnetization.

As shown in Figure 7, the antiferromagnetic exchange bias is even more obvious in complex **5**. The first step in the hysteresis loops symmetrically splits to ±0.1 T, which is significantly larger than those observed for complexes **3** and **4**. It is known that complex **5** is isostructural to complex **3** with Cl^- replaced by Br^-. The nonclassical H···Br contacts in complex **5** have about the same distance as H···Cl in complex **3**, whereas the closest Br···Br distances are even shorter than the closest Cl···Cl distances in complex **3**. The large exchange bias in complex **5** is attributable to the larger polarity of bromide ions compared to chloride ions.

Among all of the complexes, complex **6** has the largest aliphatic groups to protect its Ni^{II}_4 cubane core, and therefore, it is expected to have the smallest exchange bias. Indeed, as shown in Figure 8, the tunneling step around zero field shows smaller splitting than any other complex in this series of complexes. A precise measurement of the exchange bias can

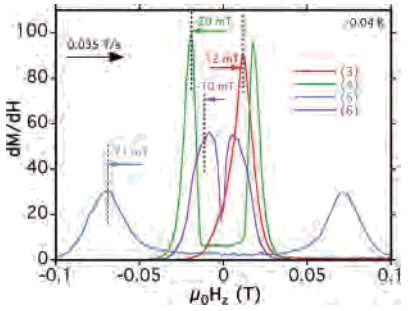

Figure 9. Plot of the first derivative (d*M*/d*H*) of the magnetization versus magnetic field for a single crystal of each **3**−**6** close to zero field. The field was swept from −1 to +1 T at a field sweep rate of 0.035 T/s. Complexes clearly **4**−**6** show an antiferomagnetic exchange bias of about −20, −71, and −10 mT, respectively. Complex **3** presents a ferromagnetic intermolecular coupling of about 12 mT.

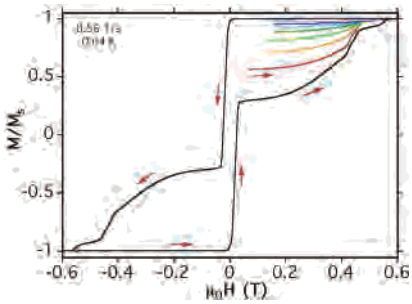

Figure 10. Hysteresis loops of a single crystal of [Ni(hmp)(dmb)Cl]$_4$ (**3**). The magnetic field is oriented parallel to the easy axis of the crystal at a scan rate 0.56 T/s at 0.004 K. The black line represents the major loop, and the colored lines represent minor loops.

be obtained by examining the first derivative (d*M*/d*H*) of the magnetization versus magnetic field close to zero field for the single crystals of complexes **3**−**6** (see Figure 9). The field was swept from −1 to +1 T at a field sweep rate of 0.035 T/s. Complexes **4**−**6** clearly show antiferromagnetic exchange biases of about −20, −71, and −10 mT, respectively, whereas complex **3** presents a ferromagnetic intermolecular coupling of about 12 mT. Except for complex **5**, which has bromide ligands, the absolute value of the exchange bias seems to parallel the order of nonclassical hydrogen-bonding contact distances.

Detailed Study of the Magnetization Hysteresis for Complex 3. Because [Ni(hmp)(dmb)Cl]$_4$ (**3**) has negligible intermolecular magnetic exchange interactions as evidenced by the absence of an exchange bias in its hysteresis loop (Figure 5) and because complex **3** has only one unique high-symmetry Ni_4 complex in its crystal, it was decided to take a closer look at the magnetization hysteresis loops for this complex. Experiments were carried out on a single crystal with a micro-SQUID energized such that the magnetic field was oriented parallel to the easy axis of the crystal using the transverse field method.[39] Figure 10 illustrates some of the hysteresis data collected for this interesting SMM. The black curve describes the main loop that was obtained during a 0.56 T/s scan at 0.04 K. The most striking features of this hysteresis loop are the steep steps observed at zero field. These precipitous steps result from fast ground-state quantum tunneling (QTM) between the $M_s = \pm 4$ states. The occurrence of ground-state QTM at zero magnetic field means

that intermolecular magnetic exchange interactions have been largely turned off. Upon scanning the field to larger values, two fast relaxation processes are observed at about 0.40 and 0.55 T; these two step features have been found to be reproducible for different crystals.

To explore the nature of the step features occurring at 0.40 and 0.55 T, additional experiments were performed. Minor hysteresis loops were traced out by starting with different initial magnetization values. The colored lines in Figure 10 represent the results of this experiment. Two features resulting from these experiments should be noted. First, when we scan backward from 0.60 T to zero field, a slight decay of magnetization away from its saturation value is observed. It is also found that the higher the initial value of the magnetization is, the smaller the decay is found to be. Second,[41] the fact that the step feature seen at 0.43 T is reproducible with different initial magnetization values suggests that this step is not due to a thermal avalanche process. However, this step at 0.43 T is not a quantum tunneling process from the ground state ($M_s = -4$) to an excited state ($M_s = +3$). This point can be confirmed if we substitute the value of 0.43 T into the expression for the Zeeman energy $E = g\beta H$ with the value $g = 2.26$ obtained from the high-frequency EPR (HFEPR) data;[42] a value of $D = -0.46$ cm^{-1} was obtained. This value is smaller than the D value obtained from reduced-magnetization and HFEPR experiments. Also, the step at 0.43 T has less amplitude than the step at zero field but does not reach the magnetization saturation value. Because the rate of the second resonance tunneling should be higher than the rate of the first resonant tunneling at zero field, the lower magnetization relaxation rate at 0.43 T indicates that the step in the range of 0.42−0.45 T does not result from a single-molecule tunneling process. Judging from the above experiments, it is more reasonable to suggest that the relaxation associated with the 0.43 T step is due to a spin−spin cross relaxation (SSCR) process.[28]

As the magnetic field is swept to a larger value, a reproducible small step is also observed around 0.55 T. Because its initial value is very close to the saturation magnetization, it is very difficult to estimate the relaxation rate for this step feature. However, substituting the value of the magnetic field (0.55 T) into the expression for the Zeeman energy $E = g\beta H$ with $g = 2.26$, the separation between this step and the ground-state quantum tunneling transition is calculated to be 0.58 cm^{-1}. This fully agrees with the D value obtained from HFEPR (average $D = -0.59$ cm^{-1}) and the reduced-magnetization ($D = -0.6$ cm^{-1}) experiments (vide infra). Therefore, this step at 0.55 T can be assigned as the second resonant quantum tunneling transition from the $M_s = -4$ to the $M_s = +3$ state.

To see these fine structures in the hysteresis loops clearly, the first derivative of the magnetization versus magnetic field

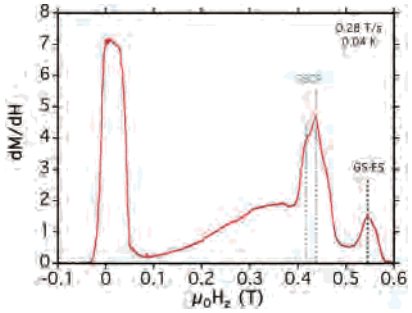

Figure 11. Plot of the first derivative (dM/dH) of the magnetization versus magnetic field for a single crystal of [Ni(hmp)(dmb)Cl]$_4$ (**3**), where the magnetic field is oriented parallel to the easy axis of the crystal.

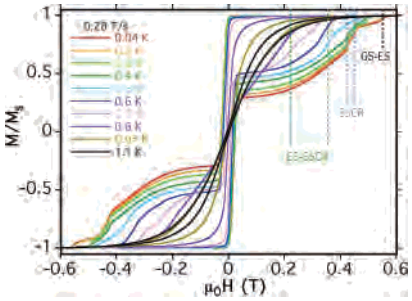

Figure 12. Magnetization hysteresis loops of a single crystal of [Ni(hmp)(dmb)Cl]$_4$ (**3**) measured in the temperature range of 0.04−1.1 K at a scan rate 0.28 T/s. The external magnetic field is oriented parallel to the easy axis of the crystal.

curve was taken. The results are shown in Figure 11, for which a scan rate of 0.28 T/s was employed. Four important features are observed in this plot. The most striking feature is the large peak at zero field that corresponds to the ground-state QTM. The high intensity of this peak reflects the high tunneling rate. The bandwidth of this peak reveals that there are some residual dipolar and magnetic exchange interactions within the crystal that have not yet been entirely turned off by the bulky aliphatic chain on the alcohol ligand. The remaining interaction estimated by the bandwidth (0.06 T) is about 0.3−0.4 K. This is very close to the magnetic ordering temperature of 0.28 K observed in the ac susceptibility experiment (vide infra).

The second largest peak observed in Figure 11 is the one at 0.43 T. This peak was tentatively assigned above to be an SSCR process. If the field is increased to 0.55 T, there is a small but obvious peak. Judging from the D and g values obtained from the HFEPR data, this peak is assigned to be the second tunneling transition (from $M_s = -4$ to $M_s = +3$).

Similar results were obtained for experiments at different temperatures and scanning rates. In Figure 12, we present the hysteresis loops obtained at a 0.28 T/s scan rate in the temperature range of 0.04−1.1 K. Above 0.7 K, the hysteresis loop due to a phonon bottleneck process is seen. As the temperature is decreased, the area enclosed in the hysteresis loop increases. It can be seen that the fine structures of hysteresis loops obtained at a scan rate of 0.28 T/s are essentially the same as those obtained at 0.56 T/s. This reproducibility reveals that these fine-structure features are not random events. Below 0.2 K, both ground-state and second resonance quantum tunneling processes can be clearly observed in both the 0.28 and 0.56 T/s scan rate runs.

(41) del Barco, E.; Hernandez, J. M.; Sales, M.; Tejada, J.; Rakoto, H.; Broto, J. M.; Chudnovsky, E. M. *Phys. Rev. B* **1999**, *60* (17), 11898−11901.

(42) Lawrence, J.; Yang, E.-C.; Edwards, R. S.; Olmstead, M. M.; Ramsey, C.; Dalal, N.; Gantzel, P. K.; Hill, S.; Hendrickson, D. N., manuscript in preparation.

Hysteresis loops were also investigated at constant temperature with different scan rates. Figure 5 illustrates the results obtained at different scan rates ranging from 0.02 to 0.28 T/s at 0.04 K. Obviously, the greater the scan rate, the larger the area enclosed in the hysteresis loop. A large amplitude of magnetization change at zero field corresponding to the ground-state QTM process is observed for all of the scan rates. However, the second resonant QTM transition is not seen until the scan rates are above 0.14 T/s. As the scan rate is decreased and the magnetic field is allowed to reside for a longer time in the tunneling window, steeper magnetization transitions are seen at zero field for lower scan rates. Analogous to the frequency dependence seen in the out-of-phase ac susceptibilities for SMMs, the fact that the hysteresis loops are scan-rate-dependent also supports the conclusion that complex **3** has the intrinsic properties of an SMM.

As we show in this article, there are several reasons why we are convinced that all six Ni_4 complexes are SMMs: (1) The complexes exhibit magnetization relaxation. (2) The complexes exhibit hysteresis in their magnetization versus magnetic field response, (3) The complexes show quantum tunneling of the magnetization. This is evidenced both by the steps observed in the hysteresis plots and by the temperature-independent rate of magnetization reversal observed (vide infra) at the lowest temperatures. (4) As we have shown, the magnetization hysteresis does not result from a phonon bottleneck. (5) The magnetization hysteresis is not due to a magnetic ordering, i.e., a phase transition to a magnetically ordered phase. The Ni_4 complexes continue to tunnel rapidly down to the lowest temperature of 0.04 K. Magnetic ordering would stop the magnetization tunneling.

Detailed Study of the Magnetization Hysteresis for Complexes 4 and 6. If one compares the hysteresis loops observed at 0.04 K, it is found that the first step in the hysteresis loop is steeper in complex **4** than in complex **3**. In addition, the loops of complex **4** are more closed at zero field than those of complex **3**. This means that the QTM process in complex **4** is faster than that in complex **3**. From the structural data, it is known that the two crystallographically independent molecules in the crystal of complex **4** have a symmetry lower than S_4. One Ni_4 complex has C_2 symmetry, and the other has only C_1 site symmetry. A reduction in crystal site symmetry leads to an increase in transverse zero-field interactions and a higher rate of QTM for complex **4** compared to complex **3**.

Because fast tunneling blocks a detailed study of the fine structure associated with the hysteresis loop for complex **4**, another experiment was designed to examine the SMM behavior of this complex. In this experiment, a single crystal of complex **4** was cooled from 5 to 0.04 K in zero field, and then the external magnetic field was swept from 0 to 0.7 T while the scan rate was varied from 0.002 to 1.120 T/s. The results of these measurements are shown in Figure 13. Well-developed SMM-type hysteresis loops are seen in this experiment. Significant area is enclosed in the hysteresis loop, and the area increases as the scan rate is increased. It can be seen that two steps repeatedly occur in the hysteresis loop: one is around 0.47 T, and the other is around 0.58 T. It is reasonable to assign these two steps to the second resonant QTM processes (ie., the $M_s = -4$ to $M_s = +3$ tunneling) for the two crystallographically different molecules in the crystal of complex **4**. However, other mechanisms such as intermolecular spin−spin cross relaxation[28] might also cause similar steps in the hysteresis loop.

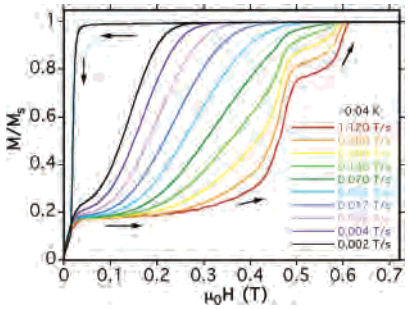

Figure 13. Minor hysteresis loops of a single crystal of [Ni(hmp)(chp)-Cl]$_4$ (**4**) at 0.04 K observed at scan rates in the range of 0.002−1.120 T/s. Loops are obtained by starting the scan from zero field.

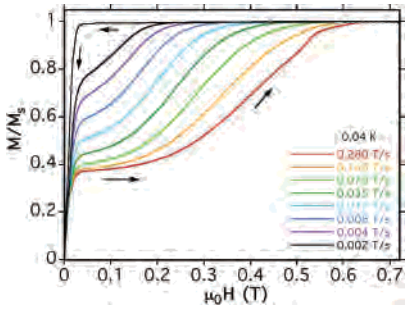

Figure 14. Minor hysteresis loops of a single crystal of [Ni(*t*-Buhmp)-(dmb)Cl]$_4$ (**6**) at 0.04 K observed at scan rates in the range of 0.002−1.120 T/s. Loops are obtained by starting the scan from zero field.

As with complex **4**, the direct observation of the fine structure in hysteresis loops for complex **6** was also blocked by the fast QTM; therefore, a similar experiment was also performed on **6**. Figure 14 gives the result of this experiment, and the SMM-type behavior such as scan-rate-dependent phenomena are clearly seen. However, further step features are not seen at scan rates up to 0.28 T/s.

Discussion of Ground-State Tunneling. It is clear that [Ni(hmp)(dmb)Cl]$_4$ (**3**) exhibits a relatively high rate of ground-state quantum tunneling of magnetization (QTM). The abrupt step observed at zero field for complex **3** in the plot of magnetization versus magnetic field is a manifestation of this rapid QTM. A more detailed kinetic study of magnetization relaxation was conducted to gain insight into the rapid QTM in complex **3**. dc magnetization decay measurements were carried out on a single crystal of complex **3**. The experiment involved saturating the magnetization of a crystal and then turning off the magnetic field and measuring the magnetization remaining as a function of time. To obtain a semiquantitative evaluation of the magnetization relaxation rate, we first saturated the crystal sample and then turned off the magnetic field and simply recorded the time (τ) for 90% relaxation at each temperature. The 90% relaxation value was selected so that we could make measurements over a larger temperature range. Figure 15

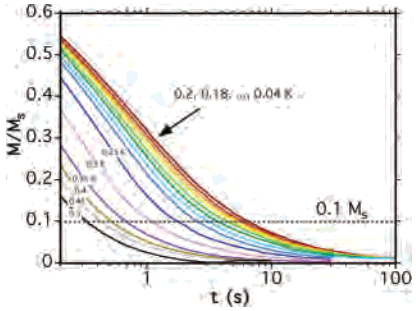

Figure 15. Magnetization relaxation versus time for a single crystal of [Ni(hmp)(dmb)Cl]$_4$ (**3**) in the temporature range 0.04−0.60 K at zero field. Relaxation times were taken as the time it took for the magnetization to decay to $0.1M_s$ (where M_s represents the saturation magnetization).

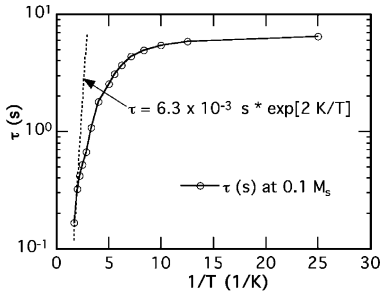

Figure 16. Temperature dependence of the logarithm of the magnetization relaxation time for a single crystal of [Ni(hmp)(dmb)Cl]$_4$ based on the data shown in Figure 12.

shows the results of dc magnetization decay experiments carried out at 14 different temperatures in the range of 0.04−0.60 K. At each temperature, there is a plot of magnetization versus time. The dashed line indicates the magnetization corresponding to 90% relaxation. Figure 16 presents an Arrhenius plot of the natural logarithm of the relaxation time versus the inverse absolute temperature. It can be seen that the relaxation time significantly increases as the temperature is decreased in the range of 0.6−0.2 K. Below 0.1 K, the relaxation rate gradually approaches a constant value. This temperature-independent relaxation rate provides a clear indication of QTM-dominant magnetization relaxation at low temperatures. The temperature independence of the rate is only explicable in terms of a ground-state QTM, where each Ni_4 SMM is tunneling between its $M_s = -4$ and $M_s = 4$ states. This further confirms the previous assignment of the step feature observed at zero field in the magnetization versus magnetic field hysteresis loops. As indicated in Figure 16, the relaxation time−temperature relationship obtained in the high-temperature limit (i.e., thermally assisted tunneling region) is $\tau = 6.3 \times 10^{-3}\exp(2/T)$ s, where τ is the 90% relaxation time and T is the absolute temperature. It is quite amazing that the effective energy barrier, U_{eff}, is 2 K, which is considerably smaller than the 13 K ($\simeq U$) classical energy barrier obtained from the formula $U = |D|S_z^2$. This extremely low effective activation energy indicates that the quantum tunneling is very fast in this molecule and makes a significant contribution to the magnetization relaxation even at higher temperatures.

It is important to compare the rate of ground-state QTM in the Ni_4 SMM complex **3** with the rates reported for other SMMs. Table 7 provides such a comparison.[10,18,20,43−47]

Table 7. Comparison of Temperature-Independent QTM Rates

complex	QTM rate (s^{-1})	S	D (cm^{-1})	$\lvert D\rvert S^2$ (cm^{-1})	ref(s)
complex 3	2×10^{-1}	4	−0.6	9.6	this work
Mn_4 cubane[a]	3.2×10^{-2}	$^9/_2$	−0.53	10.6	10
Mn_{12}−Ac[b]	$<10^{-8}$	10	−0.46	46	43
Fe_8[c]	4.5×10^{-5}	10	−0.19	19	47
Mn_4 dicubane[d]	10^{-4}	8	−0.25	16	46
Mn_{30}[e]	10^{-6}	5	−0.51	12.8	20
Mn_{18}[f]	1.3×10^{-8}	13	−0.13	22	18, 44
Mn_2[g]	5×10^3	4	−2.3	36.7	45

[a] $[Mn_4O_3Cl(O_2CCH_3)_3(dbm)]$. [b] $[Mn_{12}O_{12}(O_2CCH_3)_{16}(H_2O)_4]$. [c] $[(tacn)_6Fe_8O_2(OH)_{12}]^{8+}$. [d] $[Mn_4(OAc)_2(pdmH)_6(H_2O)_4](ClO_4)_2$. [e] $[Mn_{30}O_{24}(OH)_8(O_2CCH_2Bu^t)_{32}(H_2O)_2(MeNO_2)_4]$; [f] $[Mn_{18}O_{14}(O_2CMe)_{18}(hep)_4(hepH)_2(H_2O)_2](ClO_4)_2$. [g] $[Mn_2(Saltmen)_2(ReO_4)_2]$.

Ground-state QTM is not measurable in the prototypical $S = 10$ SMM, Mn_{12}−Ac. This complex exhibits only thermally assisted QTM, where each molecule is excited by phonons to an excited state, from the $M_s = -10$ to the $M_s = -3$ state, for example, and then tunneling occurs between the $M_s = -3$ and $M_s = 3$ excited states. Only a lower limit can be given for the rate of ground-state QTM in Mn_{12}−Ac as $<10^{-8}$ s^{-1}. For the other SMMs listed in Table 7, Arrhenius plots of the natural logarithm of the relaxation time versus inverse temperature have been determined. In all cases, a temperature-independent magnetization rate was observed at low temperatures. This rate of ground-state QTM varies from 1.3×10^{-8} s^{-1} for the Mn_{18} SMM[44] that has a ground state with $S = 13$ and $D = -0.18$ K ($= 0.13$ cm^{-1}) to the highest rate of 5×10^3 s^{-1} for a Mn_2 complex[45] that has an $S = 4$ ground state with $D = -1.1$ cm^{-1}. The rate of ground-state QTM depends on several factors. SMMs that have ground states with large spin values will tend to exhibit the lowest rates of QTM because they have large thermodynamic barriers for magnetization reversal. A naïve anticipation would be that small-spin SMMs might be expected to exhibit the fastest QTM. Examination of Table 7 shows that there is a Mn_{30} SMM[20] that has $S = 5$ and $D = -0.51$ cm^{-1} to give a barrier of $U = |D|S_z^2 = 12.8$ cm^{-1}, which is comparable to the barrier height expected for [Ni(hmp)(dmb)-Cl]$_4$. However, this Mn_{30} SMM exhibits a low tunneling rate of 10^{-6} s^{-1}, compared to the rate of 2×10^{-1} s^{-1} for the Ni_4 SMM complex **3**.

Obviously, it is not just the height of the thermodynamic barrier that determines the rate of ground-state QTM. Basically, magnetization tunneling occurs when two equi-energy states on either side of the barrier experience an interaction that mixes the two states. The magnitude of the tunnel splitting (i.e., mixing) determines the rate of QTM.

(43) *Quantum Tunneling of Magnetization: QTM '94*; Kluwer Academic Publishers: Dordrecht, The Netherlands, 1995.
(44) Brechin, E. K.; Sanudo, E. C.; Wernsdorfer, W.; Boskovic, C.; Yoo, J.; Hendrickson, D. N.; Yamaguchi, A.; Ishimoto, H.; Concolino, T. E.; Rheingold, A. L.; Christou, G. *Inorg. Chem.*, in press.
(45) Miyasaka, H.; Clerac, R.; Wernsdorfer, W.; Lecren, L.; Bonhomme, C.; Sugiura, K.-i.; Yamashita, M. *Angew. Chem., Int. Ed.* **2004**, *43*, 2801−2805.
(46) Yoo, J.; Rumberger, E. M.; Hendrickson, D. N.; Yamaguchi, A.; Ishimoto, H.; Brechin, E. K.; Christou, G. *J. Appl. Phys.* **2002**, *91* (10), 7155−7157.
(47) Sangregorio, C.; Ohm, T.; Paulsen, C.; Sessoli, R.; Gatteschi, D. *Phys. Rev. Lett.* **1997**, *78* (24), 4645−4648.

Table 8. Spin Parameters Obtained from the One-J (T_d-Symmetry) Kambe Model

complex	g	J (cm^{-1})	S
1	2.07	+4.36	4
2	2.17	+3.65	4
3	2.02	+5.21	4
4	2.01	+5.38	4
5	2.05	+5.26	4
6	1.93	+6.55	4

dc Magnetic Susceptibility Measurements. Magnetic susceptibility data were obtained for powdered samples of complexes **1**−**6** with a 1 T magnetic field in the temperature range of 2−300 K. The $\chi_M T$ data were interpreted employing two different models, as has been reported[48] for other Ni_4 cubane complexes. The first approach employed a total symmetric model assuming T_d symmetry of the molecule with all of the Ni···Ni interactions being equivalent. This gives the spin Hamiltonian

$$\hat{H} = -2J(\hat{S}_1\cdot\hat{S}_2 + \hat{S}_1\cdot\hat{S}_3 + \hat{S}_1\cdot\hat{S}_4 + \hat{S}_2\cdot\hat{S}_3 + \hat{S}_2\cdot\hat{S}_4 + \hat{S}_3\cdot\hat{S}_4) \quad (1)$$

The Kambe technique[49] gives directly the energies in eq 2 for the 19 different spin states of a Ni_4 molecule as

$$E(S_T) = -J[S_T(S_T + 1)] \quad (2)$$

where $\hat{S}_T = \hat{S}_1 + \hat{S}_2 + \hat{S}_3 + \hat{S}_4$ to give $\hat{S}_T$ values of 4, 3, 2, 1, and 0. Substituting the energies of these 19 spin states into the van Vleck equation gives a theoretical expression for the $\chi_M T$ values of a symmetric Ni_4 molecule. The $\chi_M T$ data for the above six complexes **1**−**6** were least-squares fit to this expression to give a positive J value. The resulting J and g values for these six complexes are listed in Table 8. The positive J values indicate the presence of ferromagnetic coupling between the four Ni^{II} ions and thus give an $S = 4$ ground state for each of these six complexes.

As has been reported[48] in the literature, to account for the fact that the cubane complexes in this article actually have S_4 site symmetry, which is lower than T_d, a lower-symmetry two-J model was employed to fit the $\chi_M T$ data. The spin Hamiltonian for this case is

$$\hat{H} = -2J_1(\hat{S}_1\cdot\hat{S}_2 + \hat{S}_3\cdot\hat{S}_4) - 2J_2(\hat{S}_1\cdot\hat{S}_3 + \hat{S}_1\cdot\hat{S}_4 + \hat{S}_2\cdot\hat{S}_3 + \hat{S}_2\cdot\hat{S}_4) \quad (3)$$

With the definitions of $\hat{S}_A = \hat{S}_1 + \hat{S}_2$, $\hat{S}_B = \hat{S}_3 + \hat{S}_4$, and $\hat{S}_T = \hat{S}_A + \hat{S}_B$, the spin Hamiltonian defined in eq 3 leads to the energies of different S_T, S_A, and S_B states given as

$$E(S_T,S_A,S_B) = -J_1[S_A(S_A + 1) + S_B(S_B + 1)] - J_2[S_T(S_T + 1) - S_A(S_A + 1) - S_B(S_B + 1)] \quad (4)$$

As in the simple exchange parameter model above, the energies obtained from eq 4 were substituted into the van Vleck magnetic susceptibility equation and then used to least-squares fit the $\chi_M T$ versus temperature data for each complex.

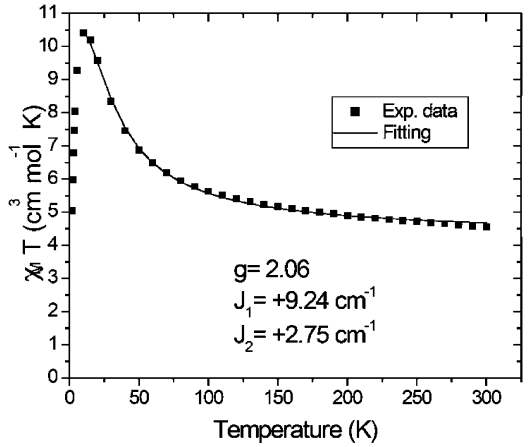

Figure 17. Plot of $\chi_M T$ vs temperature for a polycrystalline sample of $[Ni(hmp)(MeOH)Cl]_4$ (**1**) measured in a 10-kG field. The solid line represents the least-squares fit of the data to a two-J Kambe model.

Table 9. Spin Parameters Obtained from the Two-J (S_4-Symmetry) Kambe Model

complex	g	J_1 (cm^{-1})	J_2 (cm^{-1})	S
1	2.06	+9.24	+2.75	4
2	2.16	+8.27	+2.26	4
3	2.02	+5.21	+5.21	4
4	2.01	+5.38	+5.38	4
5	2.05	+5.26	+5.26	4
6	1.93	+6.55	+6.55	4

Table 10. Energy Separation (cm^{-1}) between the $S = 4$ Ground State and Lowest-Lying $S = 3$ Excited State

complex	two-J model	one-J model
1	22.0	34.9
2	18.1	29.2
3	41.7	41.7
4	43.0	43.0
5	42.1	42.1
6	52.4	52.4

Figure 17 shows the fitting of the data for complex **1** as an example. The fitting parameters from this lower-symmetry model are listed in Table 9. Again, each complex is found to have an $S = 4$ ground state. As expected, the fits obtained with the two-exchange-parameter model are better than those obtained for the one-parameter model. Also, in both cases, the data were fit to ∼15 K because neither model accounts for the zero-field splitting ($D\hat{S}_z^2$) in the $S = 4$ ground state. HFEPR data will be presented in a forthcoming paper,[42] and these data allow a characterization of the spin Hamiltonian parameters.

The analysis employing the Kambe model also allows the energy separation between the ground state and the lowest-lying excited state to be evaluated by substituting the coupling constants J back into eqs 2 and 4. The results are reported in Table 10, where it can be seen that the lowest-energy $S = 3$ excited state for these Ni_4 complexes is 18−52 cm^{-1} above the $S = 4$ ground state. Zipse et al.[51] have reported high-field EPR signals for the $S = 9$ first excited

(48) Halcrow, M. A.; Sun, J. S.; Huffman, J. C.; Christou, G. *Inorg. Chem.* **1995**, *34* (16), 4167−4177.
(49) Kambe, K. *J. Phys. Soc. Jpn.* **1950**, *5*, 48.
(50) Wang, S. Y.; Tsai, H. L.; Libby, E.; Folting, K.; Streib, W. E.; Hendrickson, D. N.; Christou, G. *Inorg. Chem.* **1996**, *35* (26), 7578−7589.
(51) Zipse, D.; North, J. M.; Dalal, N. S.; Hill, S.; Edwards, R. S. *Phys. Rev. B* **2003**, *68*, 184408.

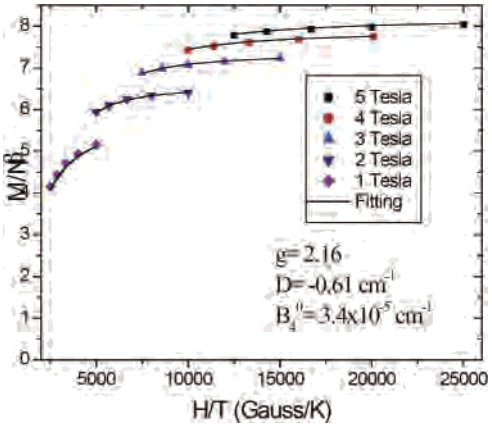

Figure 18. Reduced magnetization of a polycrystalline sample of [Ni(hmp)(dmb)Cl]$_4$ (**3**) measured with a dc magnetic field of 1−5 T in the temperature range of 2−4 K.

Table 11. Spin Hamiltonian Parameters Obtained from Least-Square Fitting of Reduced Magnetization

complex	g	D (cm^{-1})	$B_4°$ (cm^{-1})	S
1	2.09	−0.60	4.6×10^{-5}	4
2	2.12	−0.60	4.6×10^{-5}	4
3	2.02	−0.61	3.4×10^{-5}	4
4	2.11	−0.59	6.4×10^{-5}	4
5	2.18	−0.56	6.1×10^{-5}	4
6	2.13	−0.68	1.9×10^{-5}	4

state of an S = 10 Mn_{12} SMM. They determined that the $S = 9$ excited state is 24 ± 2 K above the $S = 10$ ground state.

To further confirm the spin of the ground state and the spin Hamiltonian parameters such as the g value and the axial zero-field splitting parameter, magnetization measurements were performed by applying a magnetic field of magnitude 1−5 T in the temperature range of 2−4 K. Figure 18 presents the $M/N\beta$ versus H/T plot for complex **3**, where M is the magnetization, N is Avogadro's number, β is the Bohr magneton, and H/T is ratio of the magnetic field to the absolute temperature. The solid lines in Figure 18 illustrate the full-matrix diagonalization fitting including a powder average to the experimental data. The fitting parameters are $S = 4$, $g = 2.16$, and $D = -0.6$ cm^{-1}. The results of the fitting for all complexes **1**−**6** are reported in Table 11. It is important to note that there are two crystallographically independent molecules in the crystal of both complexes **1** and **2** with the same population; therefore, the D values obtained in the reduced-magnetization fitting are actually the averages for these two molecules. The D values obtained from the fitting of reduced-magnetization data are similar to the values obtained from an analysis of HFEPR data.[42]

ac Magnetic Susceptibility Data. For many SMMs, ac magnetic susceptibility data can be employed to characterize the magnetization dynamics of molecular nanomagnets. If the frequency of the ac field encompasses a range including the rate of magnetization reversal for an SMM, then frequency-dependent in-phase and out-of-phase ac susceptibility signals are seen. However, ac susceptibility data can also be employed to determine the presence of a magnetic ordering phase transition, where, as a result of intermolecular

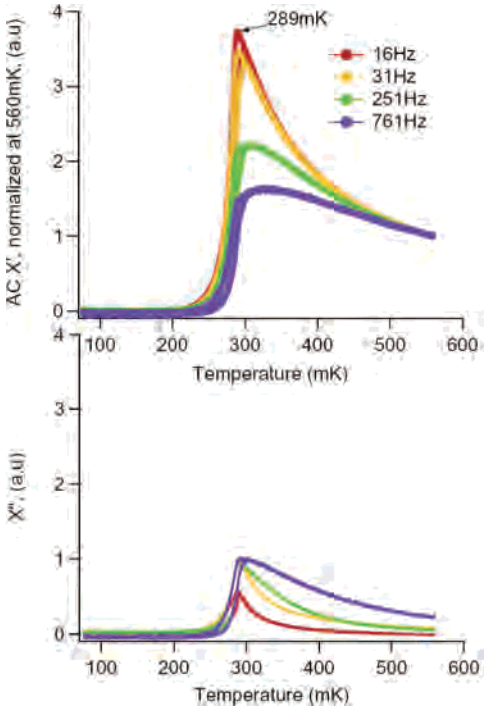

Figure 19. ac susceptibility measurements for a polycrystalline sample of complex **3** measured to the milli-Kelvin range, given in arbitrary units. The in-phase signals (χ') are shown in the top plot, and the out-of-phase signals (χ'') are presented in the bottom plot.

magnetic exchange or dipolar interactions, there is a phase transition involving a magnetic ordering of all of the SMM complexes in the crystal. At temperatures above the phase transition, the complexes are functioning independent of their neighboring complexes, but below the phase transition temperature, the intermolecular interactions become dominant, and there is a long-range magnetic ordering. Either the spins on neighboring molecules are paired to give an antiferromagnetic ordering, or the neighboring spins are ferromagnetically coupled. ac magnetic data were collected for complexes **1**, **3**, **4**, and **6** to determine whether magnetization dynamics of individual SMMs could be seen or to determine the temperatures at which magnetic ordering is seen. Figure 19 presents the ac susceptibility data collected for a polycrystalline sample of [Ni(hmp)(dmb)Cl]$_4$ (**3**) measured in an ac field oscillating in the frequency range of 16−761 Hz. As the temperature is decreased, it can be seen that the in-phase susceptibility at each frequency increases until 289 mK, below which χ' decreases rapidly essentially to zero. There is little frequency dependence, but the onset of the abrupt decrease in χ' occurs at 289 mK essentially independent of the ac frequency. In concert with the changes in the in-phase signal χ', there is an increase in the out-of-phase χ'' signal seen at the same critical temperature, and below 289 mK, the values of χ'' also collapse to zero. In the crystal of complex **3**, there must be intermolecular interactions such that, below 289 mK, there is a magnetic ordering of the magnetic moments of the Ni_4 molecules. This is further substantiated by Figure 20, which shows plots of dc magnetization versus temperature measured at different values of external dc field in the range of 1.73−17.31 G. At

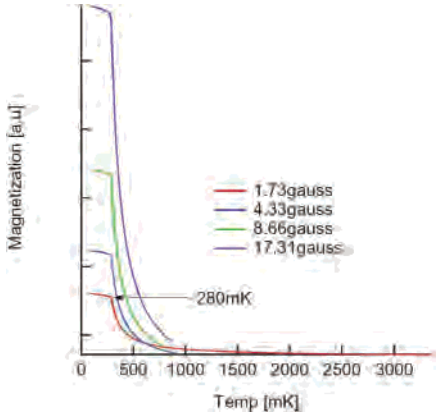

Figure 20. dc Magnetization measurements of a polycrystalline sample of [Ni(hmp)(dmb)Cl]$_4$ (**3**) given in arbitrary units. The measurements were carried out by applying dc magnetic fields in the range of 1.73−17.31 G.

each value of the external field, the dc susceptibility increases with decreasing temperature until 280 mK, where the increase in susceptibility abruptly stops.

To compare the relative strengths of intermolecular interactions in the series of Ni_4 complexes, ac magnetic susceptibility data were also obtained for complexes **1**, **4**, and **6**. It was anticipated that the MeOH complex **1** should have the strongest intermolecular magnetic exchange interactions and therefore would magnetically order at the highest temperature. Plots of the temperature dependency of the out-of-phase ac susceptibility (χ'') for [Ni(hmp)(MeOH)Cl]$_4$·xH$_2$O (**1**) are shown in Figure 21. For this complex, the abrupt fall off of the χ' signal occurs at 1100 mK (i.e., 1.10 K). Again, there is little frequency dependence. Thus, complex **1** magnetically orders at a temperature (1.1 K) that is almost 4 times higher than the 0.289 K ordering temperature seen for complex **3**.

For comparison purposes, an expanded view of the out-of-phase ac data for complex **3** is also included in Figure 21. In both cases, there is some frequency dependence, but it is *not* the simple frequency dependence seen for an isolated SMM. It is important to emphasize that the out-of-phase ac signals shown in Figure 21 are the only out-of-phase ac signals that can be seen for these two Ni_4 SMMs in the range from 300 to 0.040 K. Frequently chemists measure ac susceptibilities down to ~1.8 K. Figure 22 illustrates the ac data obtained with a Quantum Design ac SQUID in the 1.8−5.0 K range for a polycrystalline sample of complex **1**. Similar data were obtained for the other five complexes. As can be seen in Figure 22, the onset of an out-of-phase (χ_M'') ac signal is seen as the temperature is decreased to 1.8 K. This signal also seems to exhibit a frequency dependence. In many studies, this type of onset of χ_M'' signal, together with its *apparent* simple frequency dependence, would be taken as evidence for the presence of SMM behavior. However, a comparison of the data in Figure 22 measured to 1.8 K with the data measured to 0.040 K shows that there is *not* a simple frequency dependence. This raises a caveat about deciding, with ac data measured only to 1.8 K that show an onset of a χ_M'' signal, that a given complex is an SMM.

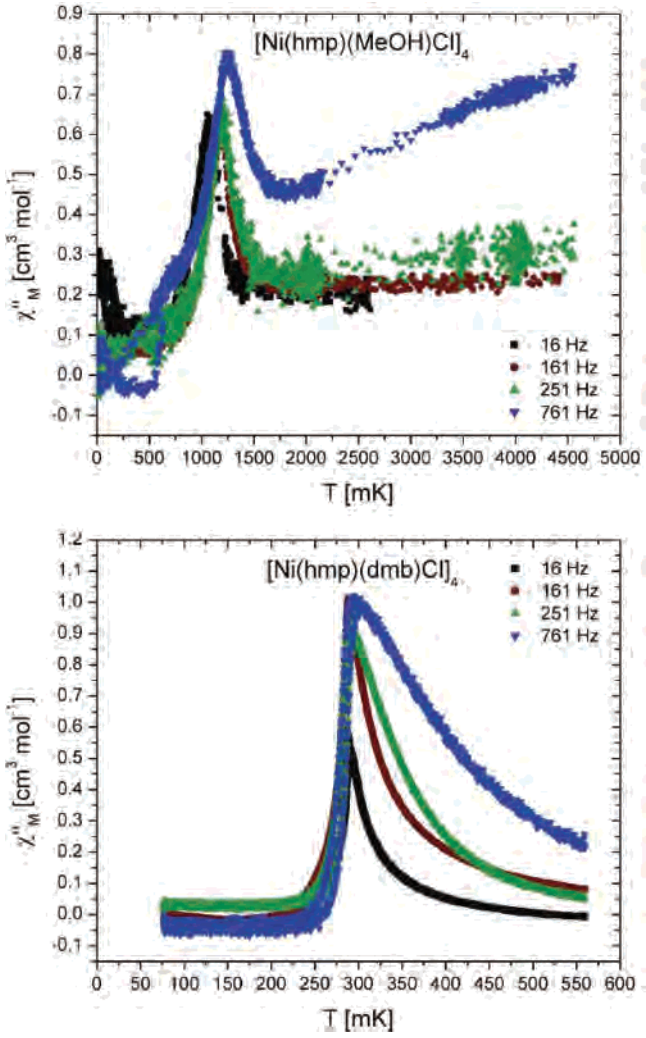

Figure 21. Out-of-phase (χ'') ac susceptibility data for (top) [Ni(hmp)(MeOH)Cl]$_4$·x(H$_2$O) (**1**) and (bottom) [Ni(hmp)(dmb)Cl]$_4$ (**3**). Data from scans with both increasing and decreasing temperature are included in the plots.

Figure 23 illustrates the χ_M'' ac data for samples of complexes **4** and **6**. Again, it is seen that the frequency dependence is not simple. Although there is some small frequency dependence, the line shape of the χ_M'' data measured at one frequency is not simple. In the case of [Ni(*t*-Buhmp)(dmb)Cl]$_4$ (**6**), the *tert*-butyl substituents on both the hmp$^-$ and the dmb ligands provide the greatest isolation between Ni_4 molecules in all six complexes. In keeping with this, the ac data for complex **6** show a χ_M'' peak at ~50 mK (Figure 23). Finally, the peak in χ_M'' for [Ni(hmp)(chp)Cl]$_4$ (**4**) is found to be ~80 mK. The peaks in χ_M'' ac data are arranged in the order complex **1** > complex **3** > complex **4** > complex **6** (see Table 12). If these χ_M'' peak temperatures reflect, in some way, intermolecular magnetic exchange interactions, then this ordering is in agreement with the expectations for intermolecular interactions obtained from the X-ray results. The order also agrees with the magnitudes of exchange bias seen in the magnetization hysteresis plots.

Figure 24 provides definitive support for the suggestion that the χ_M'' versus temperature responses found for these Ni_4 SMMs is not simply that for an isolated SMM. If only

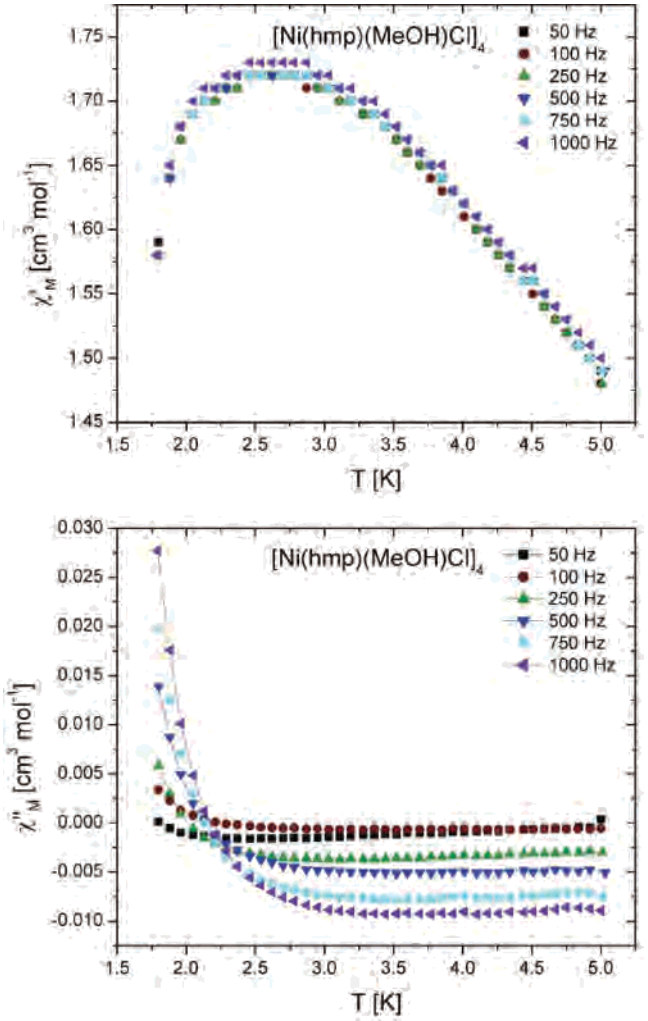

Figure 22. ac susceptibility data between 50 and 1000 Hz from 5 to 1.8 K for $[Ni(hmp)(MeOH)Cl]_4$ (**1**): (top) in-phase (χ')and (bottom) out-of-phase (χ'') ac signals.

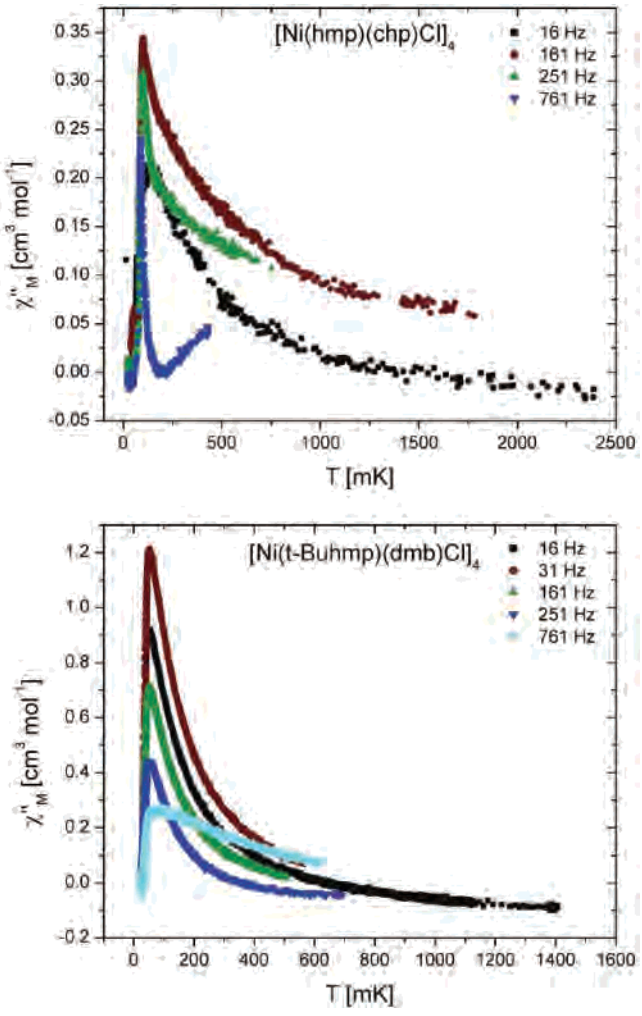

Figure 23. Out-of-phase (χ'') ac susceptibility data for polycrystalline samples of (top) $[Ni(hmp)(chp)Cl]_4$ (**4**) and (bottom) $[Ni(t\text{-}Buhmp)(dmb)Cl]_4$ (**6**).

one relaxation process is present, a plot of χ_M'' versus χ_M' (called a Cole−Cole plot) should give a semicircle. Such a behavior has been reported for several SMMs. However, as can be seen in Figure 24, when the ac susceptibility data for complex **3** is plotted in a Cole−Cole plot, the result that is obtained is far from a semicircle. Clearly, at least two different relaxation processes are contributing to these data. Further research is needed to establish the origin of the two or more relaxation processes that are contributing to the χ_M'' and χ_M' responses. It is our suggestion that there are two processes. One involves the magnetization dynamics of individual Ni_4 nanomagnets, and the other involves some magnetization relaxation of several (domains of?) Ni_4 SMMs. The magnetic ordering of regions of the crystal of a Ni_4 SMM is not static, as we observe a high rate of QTM even at 40 mK.

Concluding Comments. The four main findings in this paper are as follows: (1) the six Ni^{II}_4 complexes studied are SMMs; (2) the rate of ground-state ($M_s = -4$ to $M_s = +4$) quantum tunneling of magnetization (QTM) is quite high in the six Ni^{II}_4 SMMs; (3) intermolecular magnetic exchange interactions are present in these Ni^{II}_4 SMMs, and this affects the magnetic field (exchange bias) at which QTM occurs; and (4) changes in the steric bulk associated with the ligands can be made to modulate the intermolecular magnetic exchange interactions present in a given SMM.

In future work, we will determine the origin of the fast ground-state QTM in these Ni^{II}_4 SMMs by employing high-frequency EPR to determine the spin Hamiltonian parameters. The fact that there is fast QTM in these Ni^{II}_4 SMMs

Table 12. Magnetic Ordering Temperature of Ni_4 Complexes Based on ac Susceptibility Measurements

complex	ordering temperature (mK
$[Ni(hmp)(MeOH)Cl]_4 \cdot xH_2O$	1100
$[Ni(hmp)(dmb)Cl]_4$	290
$[Ni(hmp)(chp)Cl]_4$	∼80
$[Ni(t\text{-}Buhmp)(dmb)Cl]_4$	∼50

Table 13. Strength of Intermolecular Dipolar Interactions in Complexes **1**, **3**, **4**, and **6**

complex formula	closest intermolecular distance (Å)	closest Ni···Ni distance (Å)	dipolar interactions (mK) based on column 2	dipolar interactions (mK) based on column 3
$[Ni(hmp)(MeOH)Cl]_4$	7.2	11.4	130	33
$[Ni(hmp)(dmb)Cl]_4$	8.0	10.9	96	38
$[Ni(hmp)(chp)Cl]_4$	9.0	9.9	67	50
$[Ni(tBuhmp)(dmb)Cl]_4$	9.4	12.5	59	25

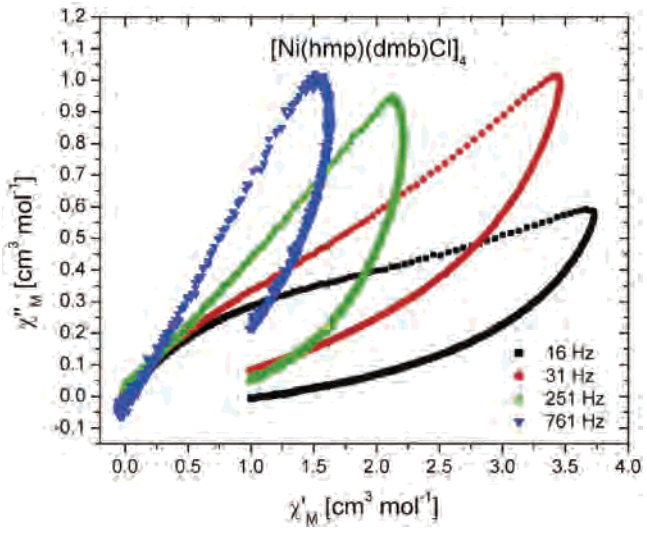

Figure 24. Cole−Cole plot for $[Ni(hmp)(dmb)Cl]_4$ (**3**). Data show four noncircular ellipsoid shapes indicating the presence of multiple processes at low temperatures.

can be further demonstrated by examining the magnetization loop for the complex $[Mn_4O_3Cl(dbm)_3(OAc)_3]$, an $S = {}^9/_2$ SMM with a thermodynamic magnetization reversal barrier of $U = 10.6$ cm^{-1}, that is comparable to the $U = 9.6$ cm^{-1} barrier found for $[Ni(hmp)(dmb)Cl]_4$ (**3**). In Figure 25 is shown the hysteresis loop of a single crystal of the $S = {}^9/_2$ SMM with the external magnetic field oriented parallel to the easy axis of the crystal. A comparison with the loops seen for complex **3** (Figures 5 and 10) shows that the $S = {}^9/_2$ Mn_4 SMM exhibits a much larger coercive field (i.e., larger area in loop) than is seen for complex **3**. This is because the rate of QTM in the $S = {}^9/_2$ Mn_4 SMM is an order of magnitude lower. It is possible to "turn on" the QTM for the $S = {}^9/_2$ Mn_4 SMM by introducing a transverse interaction that causes tunnel splitting (mixing) between the $M_s = -{}^9/_2$ and $M_s = +{}^9/_2$ states of the $S = {}^9/_2$ SMM. In Figure 25, the transverse interaction is added in the form of a transverse magnetic field, which can be seen to affect dramatically the appearance of the hysteresis loop. With such a transverse magnetic field present, the coercive field is collapsed, and the hysteresis loop for the $S = {}^9/_2$ Mn_4 SMM now looks very similar to that seen for complex **3**.

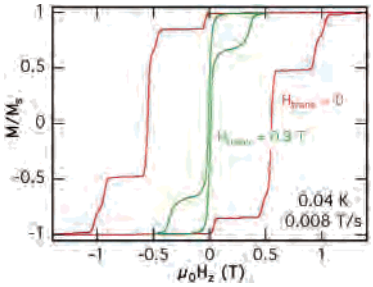

Figure 25. Magnetization hysteresis loops of $[Mn_4O_3Cl(dbm)_3(OAc)_3]$ cubane molecule with a transverse magnetic field 0.9 T (green curve) and without a transverse magnetic field (red lines) at 0.04 K. The magnetization M is plotted as a fraction of the maximum value of M_s, the saturation magnetization.

Transverse interactions present in the crystals of the Ni^{II}_4 SMMs cause the high rate of QTM. These transverse interactions either can be magnetic in origin or can arise from zero-field interactions. The transverse magnetic field can potentially arise from either external or an internal magnetic field. The fast ground-state QTM occurs in the absence of an external field (first steep hysteresis step). It is very likely that the fast QTM in Ni^{II}_4 SMMs arises from transverse zero-field interactions. Because high crystal site symmetry (S_4) is present in several of them, it is likely that it is higher-(quartic-) order transverse zero-field interactions that are most important. Furthermore, the zero-field interactions in the $S = 4$ ground state arise from a tensor projection of the single-ion zero-field interactions at each of the Ni^{II} ions in the complex. In short, the spin−orbit interactions present at each Ni^{II} ion project onto the $S = 4$ ground state of the Ni^{II}_4 complex and give fast QTM. Delineating this single-ion effect will be focus of future work.

Acknowledgment. This work was supported by the National Science Foundation.

Supporting Information Available: X-ray crystallographic files in CIF format are available for complexes **1**−**6**. This material is made available free of charge via the Internet at http://pubs.acs.org.

IC050093R